A simple model for H-2 line profiles in bow shocks

Author:

Schultz, Angie; Burton, Michael; Brand, P. W. J. L.

A Simple Model for H_2 Line Profiles in Bowshocks

A.S.B. Schultz[1], M.G. Burton[1] and P.W.J.L. Brand[2]

[1] *School of Physics, University of New South Wales, Sydney 2052, Australia*
[2] *Institute for Astronomy, University of Edinburgh, Blackford Hill, Edinburgh, EH9 3HJ, UK*

ABSTRACT

We present a model for empirically reproducing line profiles of molecular hydrogen emission in bow shocks. The model takes into account bow velocity, dissociation limit, a cooling function, viewing angle, bow shape and a limited form of extinction. Our results show that both geometrical factors and shock physics can significantly affect the profile morphology. In a companion paper we will apply this model to Fabry-Perot observations of bow shocks in the Orion BN-KL outflow.

Key words: shock waves – line:profiles – ISM:jets and outflows – molecules – stars:formation.

1 INTRODUCTION

Bow shocks are common astronomical structures – they are found around the Earth and other planets (e.g. Spreiter & Stahara 1995), around pulsars (e.g. Bucciantini & Bandiera 2001) and runaway OB stars (e.g. Noriega-Crespo et al. 1997), in merging galaxies (e.g. Markevitch et al. 2002) and planetary nebulae (e.g. Vázquez et al. 2000). They are also ubiquitous in young stellar outflows, appearing in the form of Herbig–Haro (HH) objects (see, e.g. Schwartz 1978).

Herbig–Haro objects are emission nebulae formed when the outflow from a young stellar object impacts on ambient material, shocking the outflowing and/or ambient gas. HH objects are usually rather compact (on the order of 1000 AU), appearing as clumps or knots. Well-known HH bow shocks include HH 7 (Smith, Khanzadyan & Davis 2003), HH 34 (Reipurth et al. 2002), HH 47 (Heathcote et al. 1996) and HH 1 (Bally et al. 2002).

HH objects are formed by one of three mechanisms: in the working surfaces of jets (e.g. Mundt 1985); by clumps in the outflow encountering the ambient medium ("bullets"; Norman & Silk 1979); or by the interaction of an outflow with a clumpy ambient medium ("shocked cloudlets"; Schwartz 1978). In this paper we examine how line profiles formed in the latter two mechanisms may vary with geometry and shock parameters. (In the case of HH objects formed from jets, there is the complication of a second shock from decelerated jet material as well as the the bow shock of accelerated ambient material. Emission from the two shocks may be difficult to resolve at this time.)

Our impetus for modelling these structures is the study of the array of H_2 bow shocks found in the Orion BN-KL outflow (Allen & Burton 1993; Schultz et al. 1999). These objects are too numerous and short-lived (with a cooling time of $\approx$ one year, Allen & Burton 1993) to be the result of a precessing jet. They may have been produced by "bul-

lets" ejected from a central source, or have been produced *in situ* by Rayleigh-Taylor instabilities as the outflow swept up the ambient medium (Stone, Xu & Mundy 1995). For the purposes of this paper, the precise method of bow shock production is irrelevant. We will treat the bow shocks as having been created by dense clumps moving through the ambient medium.

In the present paper we will examine the bowshocks themselves, studying the effect of bow shape, velocity, viewing angle, cooling function, dissociation and extinction on profiles of shocked emission lines. Our objective in this paper is to use the modelled line profiles to empirically constrain the bow shock geometry and the shock physics. In a subsequent paper we will compare the modelled profiles to Fabry-Perot observations of H_2 line emission in Orion BN-KL.

2 DESCRIPTION OF THE MODEL

In this model, the bow is divided into elements along the z-axis (the longitudinal axis of the bow; see Fig. 1), which are then further divided into elements in ϕ, the azimuthal angle about the z-axis. Each element acts as a thin planar shock; we do not attempt to resolve the shock front, e.g. in order to distinguish between J-shocks and C-shocks (which possess extended shock fronts). The results presented here use emission from the entire bow surface, although the model allows the selection of regions of the bow, for modelling of spatially resolved bows.

The shock is modelled as a steady-state bow moving through a stationary medium with a velocity V_{bow}. The x-y plane is tangential to the apex of the bow, with the y-axis parallel to the plane of the sky. The origin of the coordinate system is at the apex of the bow. Fig. 2 shows the geometry of the bow in the y-z plane.
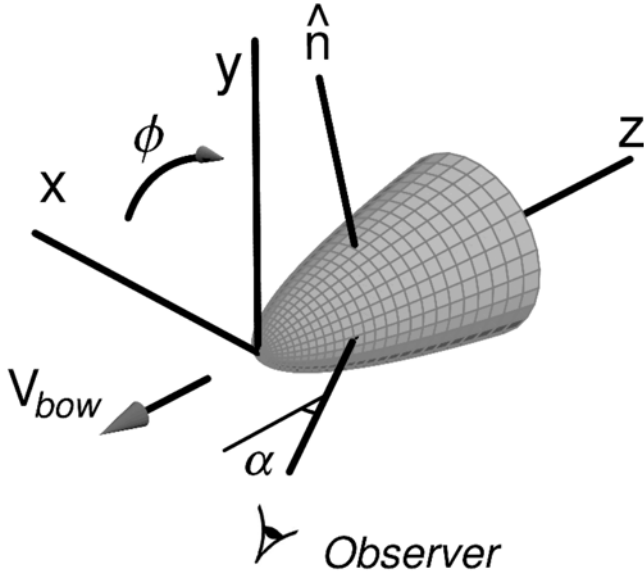
Figure 1. Three-dimensional view of the bow shock geometry. The bow moves at a speed V_{bow} in the negative z-direction; α is the angle between the observer's line of sight and the axis of the bow (the z-axis), $\hat{n}$ is the unit vector normal to the bow surface and ϕ is the longitudinal angle about the axis of the bow.

We define the direction of bow motion to be along the negative z-axis. The ambient medium impacts the bow surface at an angle ψ, where $\psi = 90$ degrees at the apex, and $\psi \rightarrow 0$ degrees toward the rear of the bow. The shock velocity is then the component of the bow velocity in the direction normal to the bow surface, given by $v_{\perp} = V_{bow} \sin\psi$. We assume that the shocked gas is "stunned", i.e. that the post-shock velocity in the direction normal to the surface is zero. This is not unreasonable, since in a strong shock the post-shock velocity of the cooled gas is of order 1/40 of the pre-shock velocity (HRH 1987; hereafter HRH). We further assume that the post-shock velocity parallel to the bow surface is unchanged, so that the gas continues to flow along the bow after it has been shocked. The post-shock gas is assumed to emit line radiation immediately and then cool. The post-shock velocity for each surface element is projected along the line-of-sight axis (see below), and the contributions from each element added to produce the line profile.

For J-shocks the stunning assumption provides a good approximation for calculating the emission because the cooling length is relatively small ($\approx$ 10 AU) and unresolved. Most of the compression of the gas (which is of the order of the square of the Mach number) takes place before any emission occurs. For C-shocks the assumption is less good, for compression takes place within the drag length, which can be up to 100 times longer than in the J-shock case. This places the C-shock width at about the current limit of spatial resolution in sources as nearby as Orion.

The flux I in each element is assumed to be proportional to $n_0 v_{\perp}{}^p$, where n_0 is the hydrogen number density. Since we are not adopting a physical size for the bow in this model, we set $n_0 = 1$. The parameter p is the *cooling function index*, which is a measure of how much of the energy of the shock goes into the excitation of a single molecular
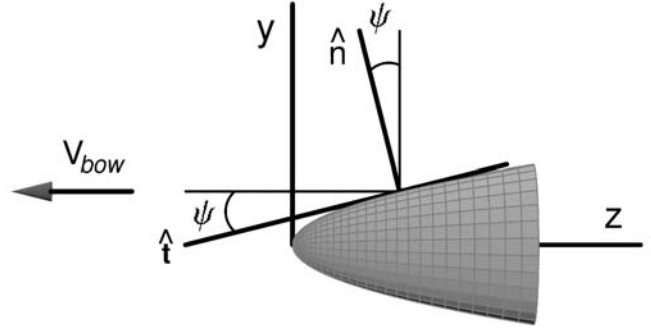

Figure 2. The geometry of the bow shock in the in the y-z plane, showing ψ, the angle between V_{bow} and the tangent to the bow surface This is also the angle between the y-axis and the normal to the bow surface.

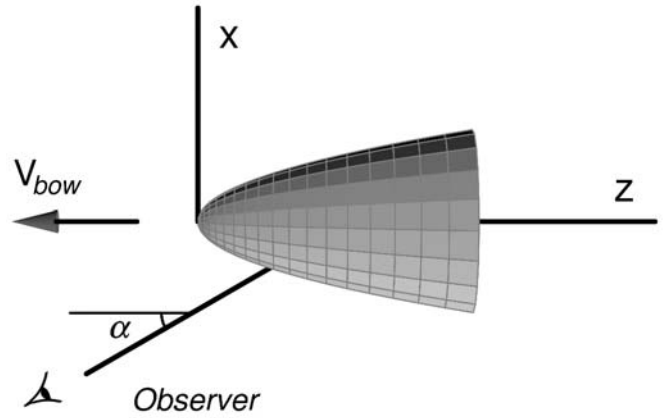**Figure 3.** The geometry of the bow shock in the in the x-z plane, showing the viewing angle, α.

line. The cooling function index has an upper limit of 3; this would be its value if all the energy of the shock went into excitation of a single H_2 line (since KE $\propto v^3$) – or was shared equally between several lines – and not into excitation of other species, grain destruction, etc. We take 1 as our lowest value for the cooling function, although in principle it has no lower bound. See § A1 for further details.

There are two cases when the emitted flux is set to zero: when $v_{\perp} \geqslant V_{lim}$, the dissociation speed of the shock; and when $v_{\perp} \leqslant V_{term}$, below which velocity the shock is not strong enough to produce excited vibrational states of H_2. We assume $V_{term} = 5$ km s^{-1} (see Burton, Hollenbach & Tielens 1992).

Fig. 3 shows the relationship of the observer to the bow. The x-axis is defined such that the observer's line of sight lies in the x-z plane, making an angle α with the z-axis. The observed radial velocity of a bow element is given by

$$v_r = V_{bow}[\cos\psi(\sin\alpha\sin\psi\cos\phi + \cos\alpha\cos\psi) - \cos\alpha], \quad (1)$$

where the radial velocity direction is defined in the conventional manner, with negative velocities toward the observer (see §A2 for the derivation of Eqn. 1).

The line profile is produced by summing the flux from all bow elements having a radial velocity v_r (actually each v_r is a small range of velocities; see §A5), and plotting I

vs v_r. The resulting curve may be treated with Gaussian, Lorentzian, or triangular smoothing, or left unsmoothed. All the curves shown here have been smoothed with a Lorentzian of 14 km s⁻¹ FWHM in order to compare the models with our Fabry-Perot observations (see Paper II).

The model is subject to certain limitations. Most of the chemistry and physics of the shock is expressed by the cooling function index, p, which determines how much of the shock energy goes into producing a single emission line (see §3.3). In reality, of course, the kinetic energy is released as a wide variety of atomic and molecular lines, as well as in grain heating and destruction. For other lines, or species, different values of p may be appropriate. Comparison of our empirical model with observations will indicate the permitted range of the cooling function index.

Since we do not adopt specific physical shock parameters, we cannot make flux comparisons between models, or use observed fluxes to constrain models. Comparisons between basic profile morphologies can still be made, as can comparisons of the effects of our modelled parameters. It is the purpose of this paper to show how these influence the observed line profile, and thus empirically constrain the quantities which produce it. In particular, we examine the effects of orientation, bow speed, bow shape and differential extinction on the line profile. We also investigate the sensitivity of the profile to gas cooling mechanism.

3 MODEL PARAMETERS

We have examined the results of this model for changes in the following parameters:

- $V_{bow} = 50, 100, 150$ and 200 km s⁻¹

The bow speed is simply the speed of the bow through the medium. See §3.1.

- parabolic, cubic, Raga and HRH "Shape A" bow shapes:

Cubic : $z = R^3$

Parabolic : $z = R^2$

Raga : $z = \gamma R^2 + \gamma^3 \beta R^4$;
where $\gamma = 0.42$ and $\beta = 1.84$

HRH "Shape A" : $z = \gamma R^2 + \gamma^3 \beta R^4$;
where $\gamma = 0.42$ and $\beta = 13.5$

In each case z is the distance along the longitudinal axis of the bow and R is the bow radius at that distance. The shapes are shown in Fig. 4 (see also Fig. 14) and are described more fully in §3.2.

- cooling function index $p = 1$, 2 and 3

In our model the flux $I \propto v_\perp{}^p$, where we have termed p the cooling function index. This parameter encapsulates the shock physics, indicating the amount of shock energy which results in a particular molecular transition. The resultant line emission from this transition radiatively cools the gas (see §3.3). When compared with observed line profiles, our model can be used to constrain the permitted values of p, and therefore evaluate the merits of various shock cooling models. This can be done by calculating the effective value of
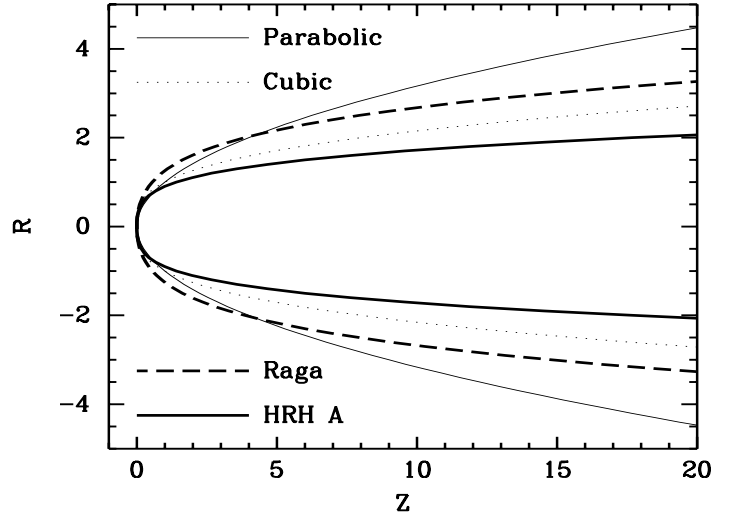

Figure 4. A comparison of the four bow shapes.

the cooling index for a particular line in a particular model, then examining whether the model profiles for that index resemble the observed profile.

- viewing angle $\alpha = 0, 30, 60$ and 90 degrees

This is the angle (in the x-z plane) of the axis of the bow with respect to the observer's line of sight. An α of 0 degrees means the bow is viewed head on; at $\alpha = 90$ degrees the bow is viewed from the side. See §3.4.

We also investigated the effects of dissociation (§3.5), comparing bows with no dissociation to those with a dissociation velocity of 50 km s⁻¹, which is typical for C-shocks (Draine, Roberge & Dalgarno 1983). Local conditions might increase the dissociation velocity, however; Smith, Brand, & Moorhouse (1991) examine a model for C-shocks in dense gas with high Alfvén speed where the dissociation speed can be as large as 200 km s⁻¹.

Finally, we examined two extinction cases: no extinction, and total extinction within the bow (§3.6). The latter case assumes that the "far" side of the bow – that is, those portions hidden from the observer – suffers complete extinction. Comparison of these extreme cases allows the assessment of the effects of partial extinction on line profiles. The effects of foreground extinction are not considered.

The complete results are shown in Figures 5 through 8. Each figure contains profiles for a single bow shape. Each of the four subfigures (a) – (d) within a figure presents the results from a single V_{bow}. A row of plots within a subfigure shows the effects of α increasing from left to right ($\alpha = 0, 30, 60, 90$), with the plots in each row having a common value of p. The value of p increases going from top to bottom in a subfigure ($p = 1, 2, 3$).

All plots show intensity on the y-axis and velocity on the x-axis. The velocity range is the same for all plots within a subfigure, since they are all at the same V_{bow}. The curves have been normalised to the value of the highest peak *in each plot*. Therefore intensities can be legitimately compared only within the curves in a single plot. The velocities have been normalised to v/V_{bow}.

Within each of these plots, a heavy solid line represents a model with no dissociation and no extinction; a dashed
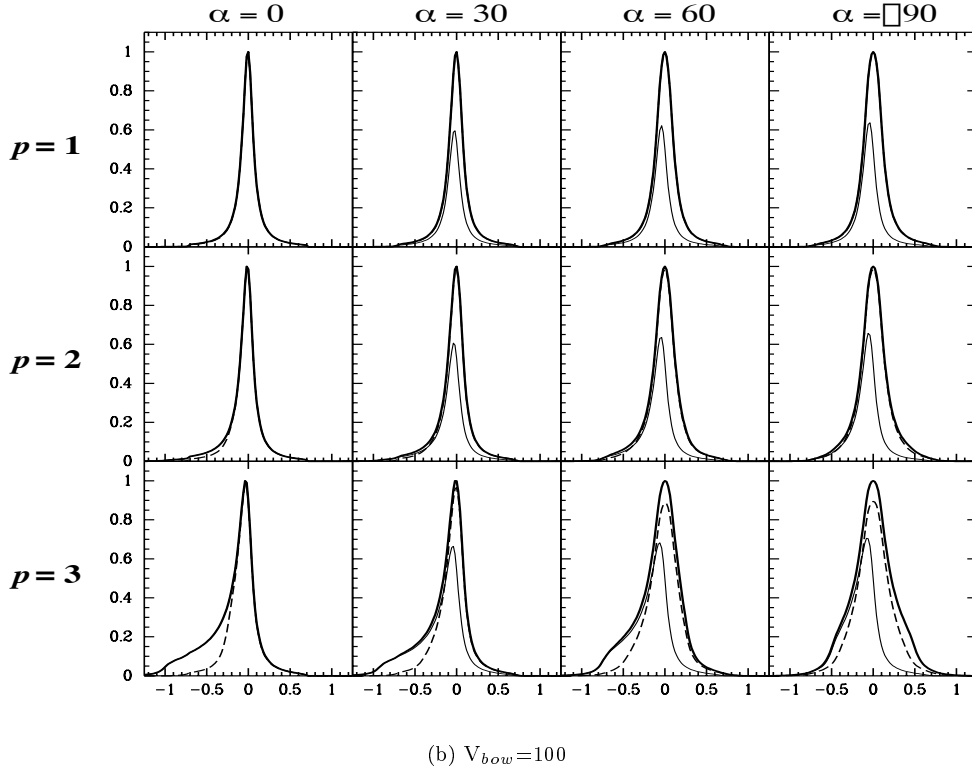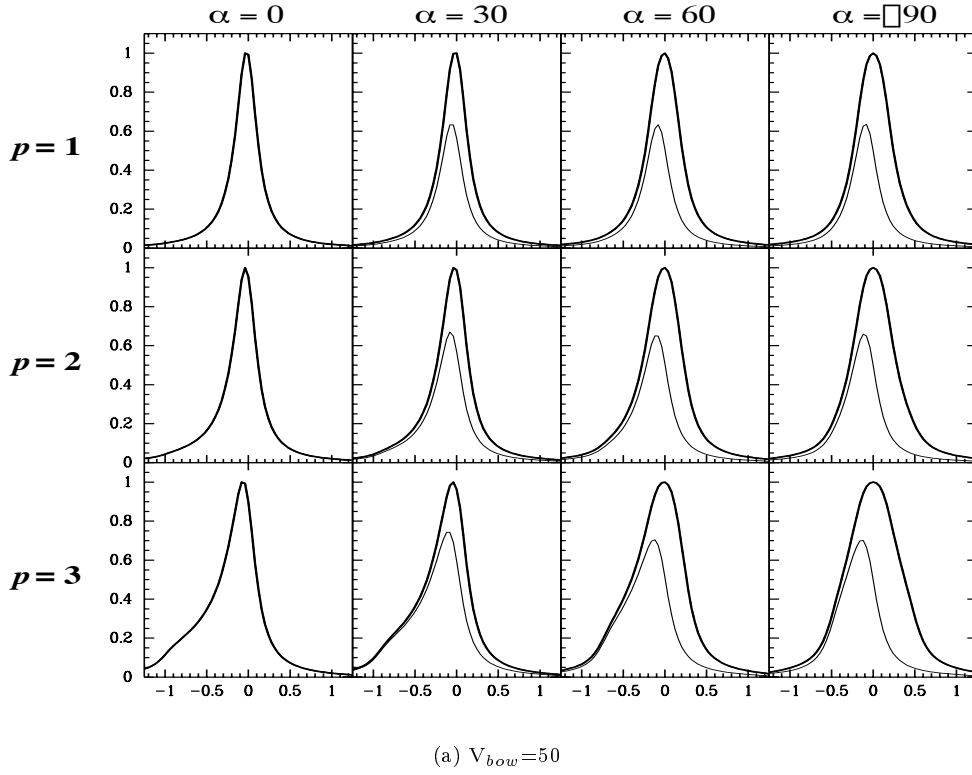
(a) $V_{bow}=50$

(b) $V_{bow}=100$

Figure 5. Line profiles illustrating changes in viewing angle α and cooling function index, p, for a parabolic bow. Heavy solid line: no extinction, no dissociation; light solid line: extinction, no dissociation; dashed line: no extinction, dissociation with $V_{lim}=50$. The panels (a) and (b) are for bow speeds of 50 and 100 km s^{-1}, respectively. Each grid is comprised of 12 plots. Across the page α increases from 0 to 30, 60 and 90 degrees; down the page the values of p are 1, 2 and 3.

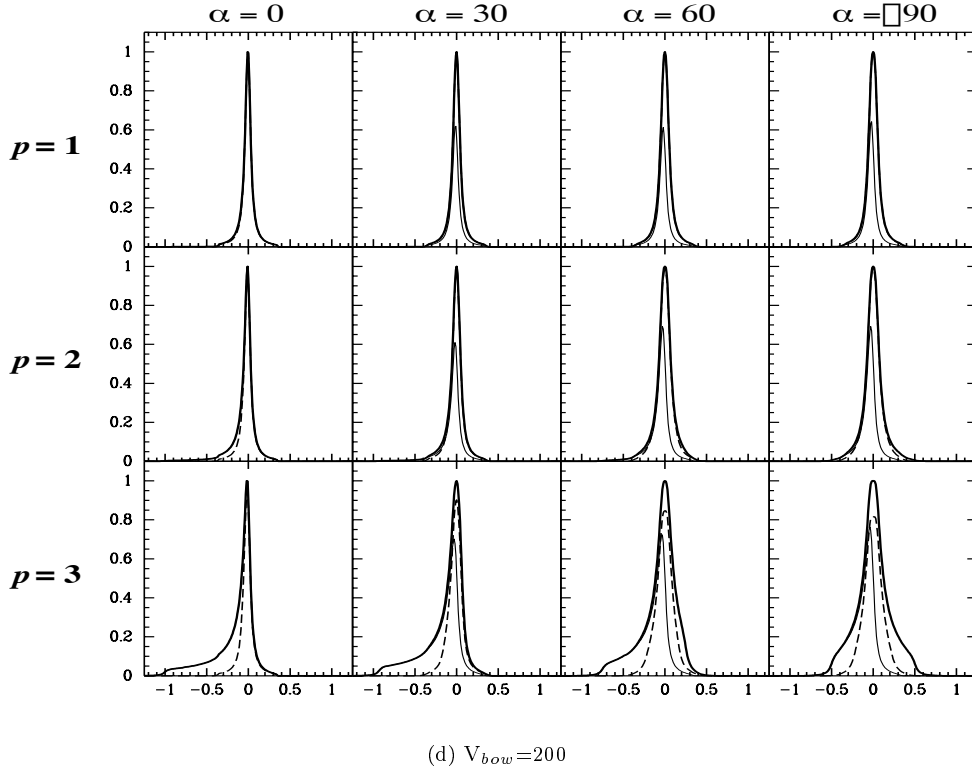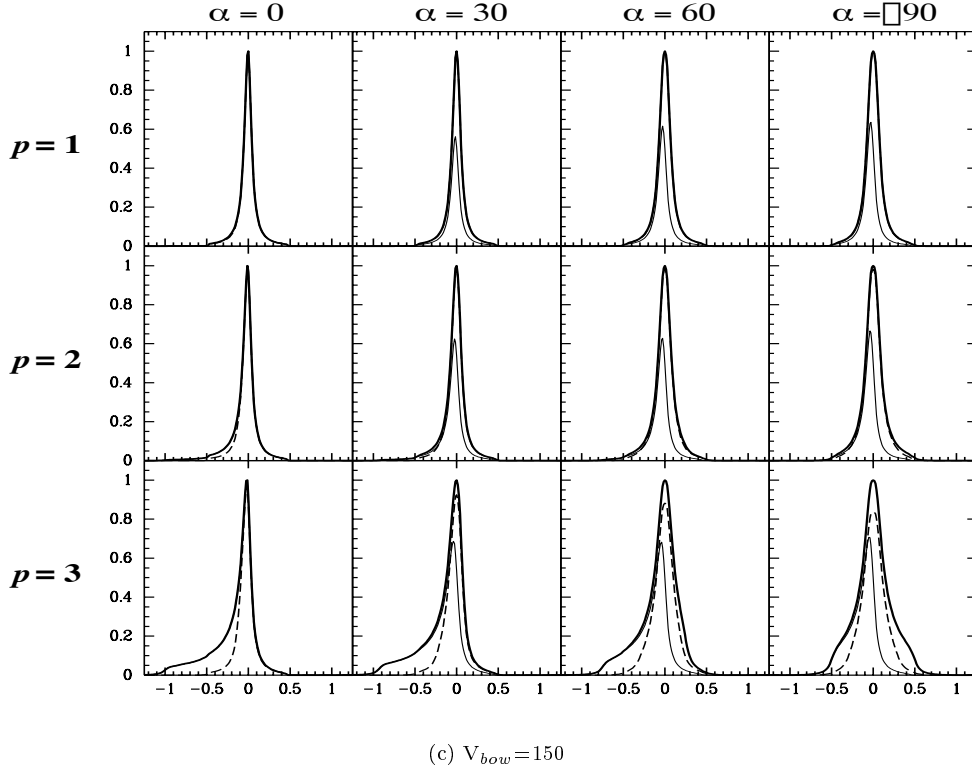(c) V$_{bow}$=150

(d) V$_{bow}$=200

Figure 5. (continued) As in the previous page, but for bow velocities of 150 and 200 km s^{-1} in panels (c) and (d), respectively. Heavy solid line: no extinction, no dissociation; light solid line: extinction, no dissociation; dashed line: no extinction, dissociation with V$_{lim}$=50.
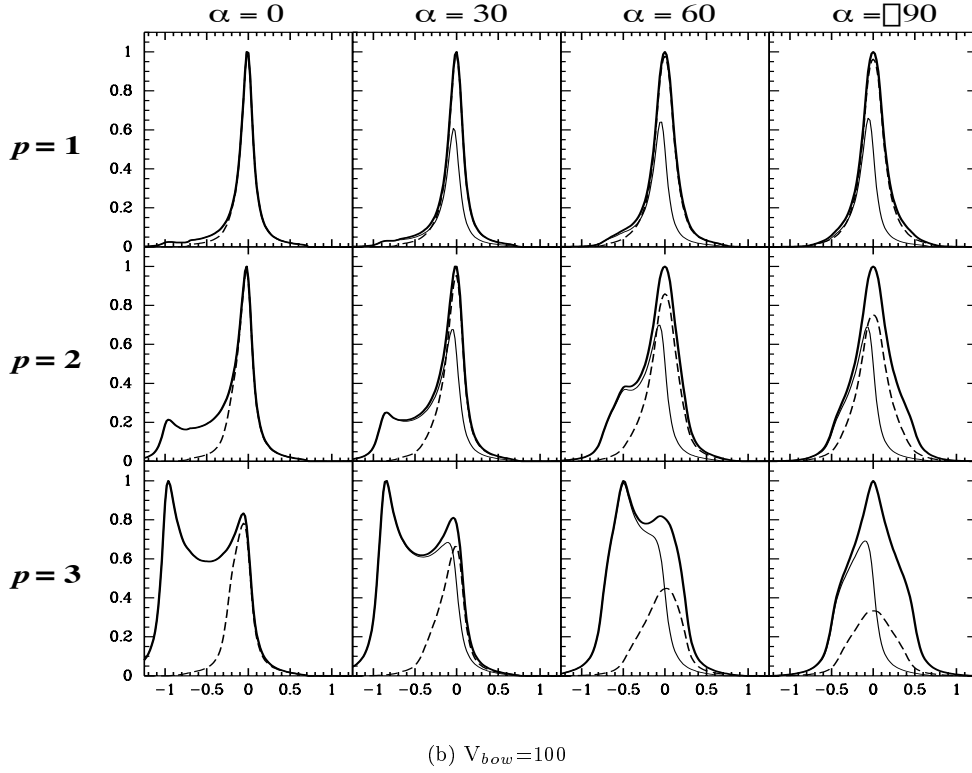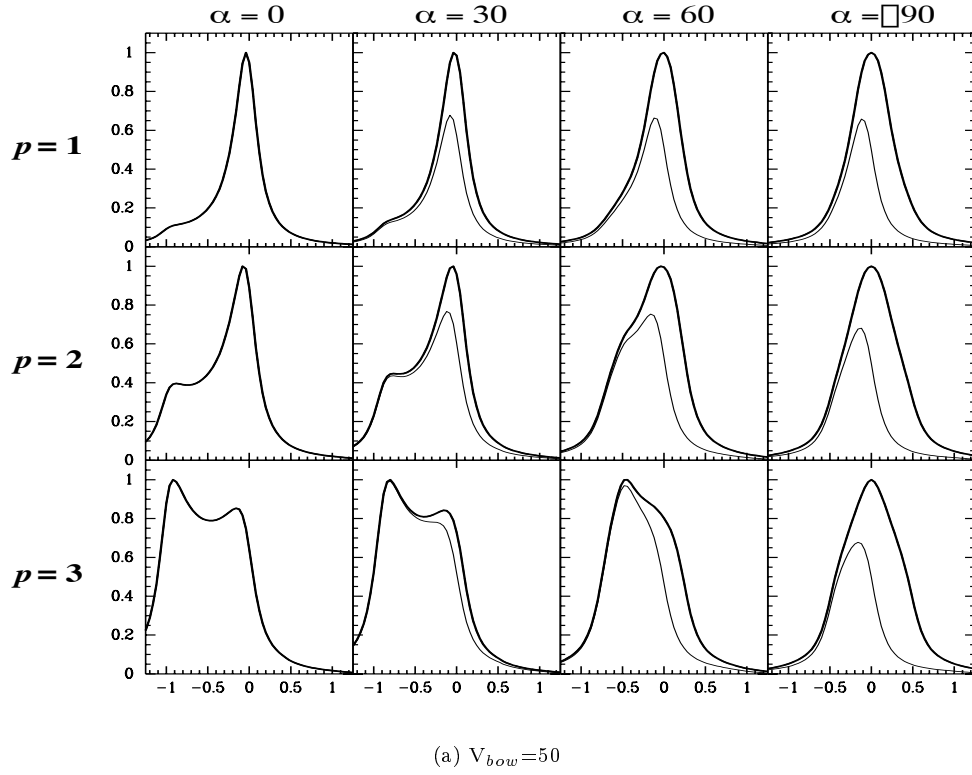
(a) V$_{bow}$=50

(b) V$_{bow}$=100

Figure 6. As in Fig. 5(a) and (b), but for a cubic bow. Heavy solid line: no extinction, no dissociation; light solid line: extinction, no dissociation; dashed line: no extinction, dissociation with V$_{lim}$=50.

(c) V$_{bow}$=150

(d) V$_{bow}$=200

Figure 6. (continued) As in the previous page, but for bow velocities of 150 and 200 km s^{-1} in panels (c) and (d), respectively. Heavy solid line: no extinction, no dissociation; light solid line: extinction, no dissociation; dashed line: no extinction, dissociation with V$_{lim}$=50.
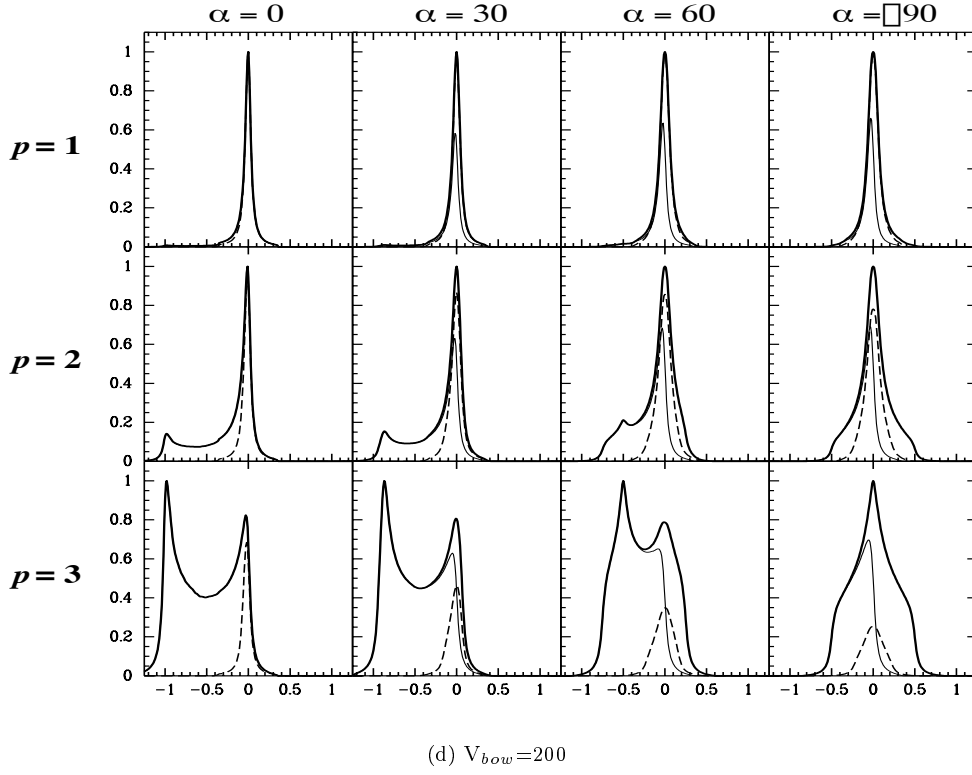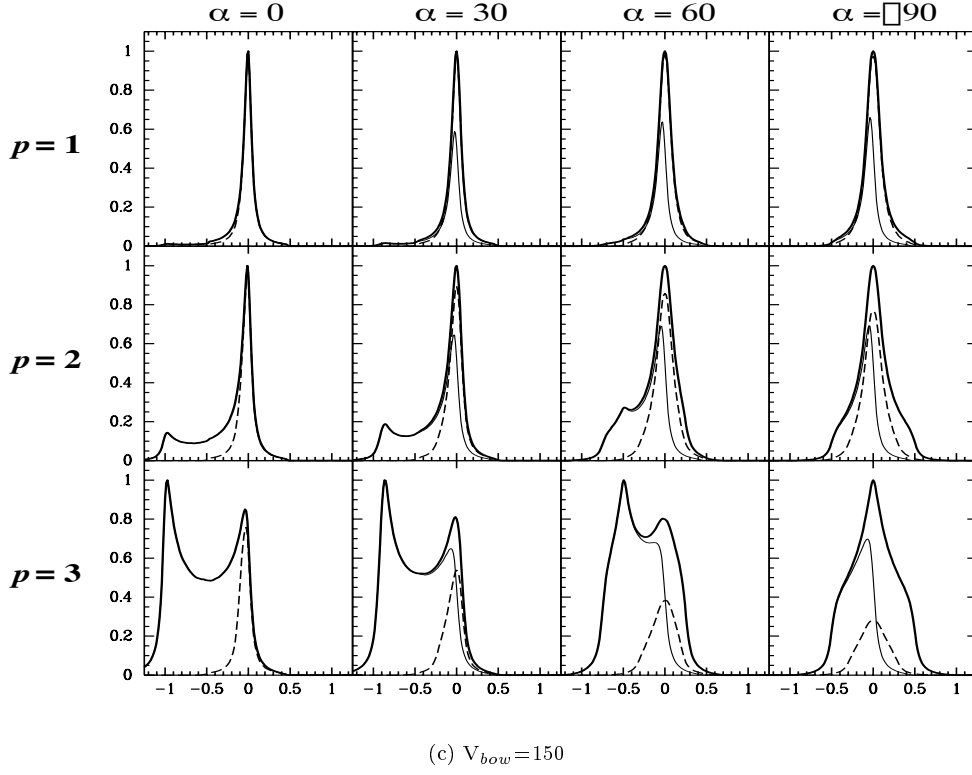
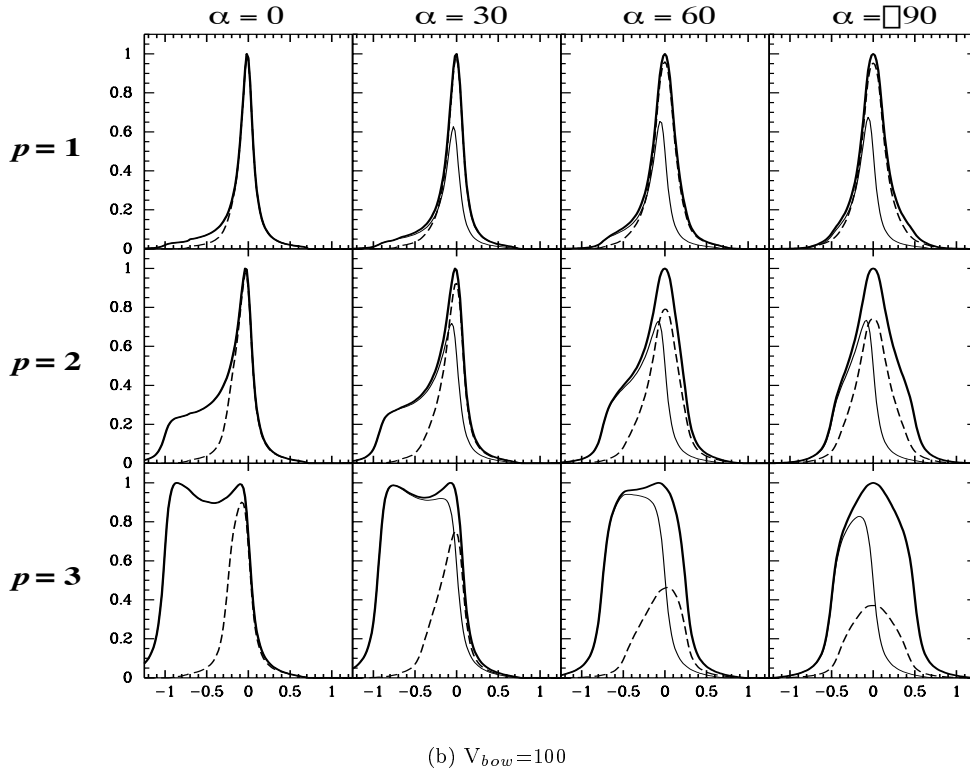(a) V_{bow}=50

(b) V_{bow}=100

Figure 7. As in Fig. 5(a) and (b), but for a Raga bow. Heavy solid line: no extinction, no dissociation; light solid line: extinction, no dissociation; dashed line: no extinction, dissociation with V_{lim}=50.

(c) V$_{bow}$=150

(d) V$_{bow}$=200

Figure 7. (continued) As in the previous page, but for bow velocities of 150 and 200 km s^{-1} in panels (c) and (d), respectively. Heavy solid line: no extinction, no dissociation; light solid line: extinction, no dissociation; dashed line: no extinction, dissociation with V$_{lim}$=50.
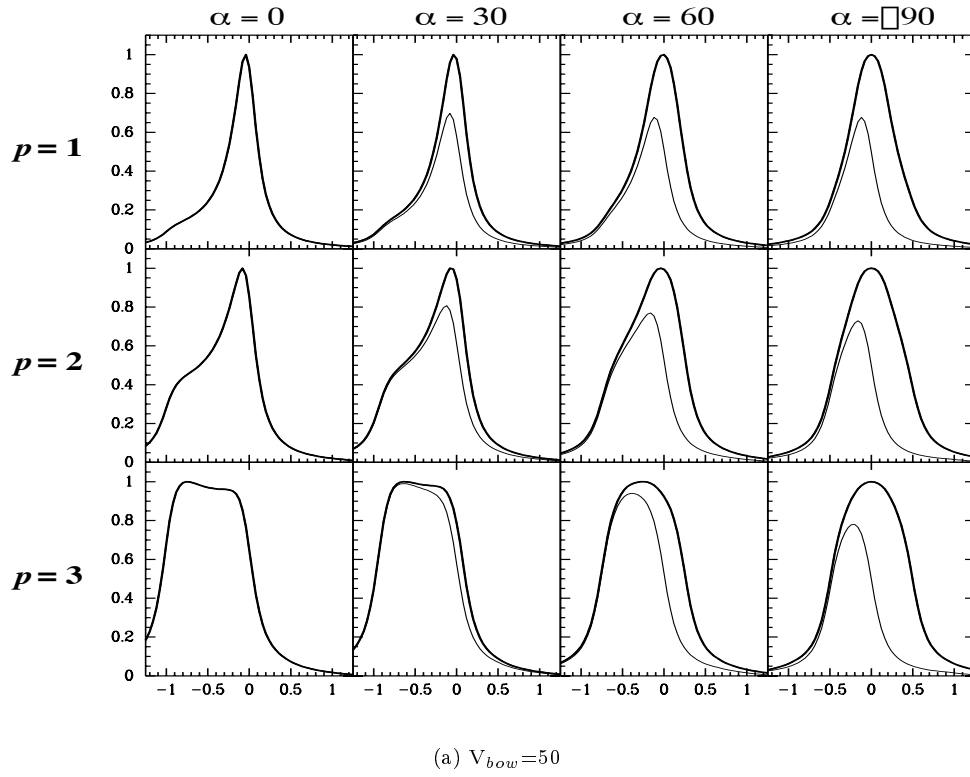
(a) V$_{bow}$=50

(b) V$_{bow}$=100

Figure 8. As in Fig. 5(a) and (b), but for an HRH A bow. Heavy solid line: no extinction, no dissociation; light solid line: extinction, no dissociation; dashed line: no extinction, dissociation with V$_{lim}$=50.
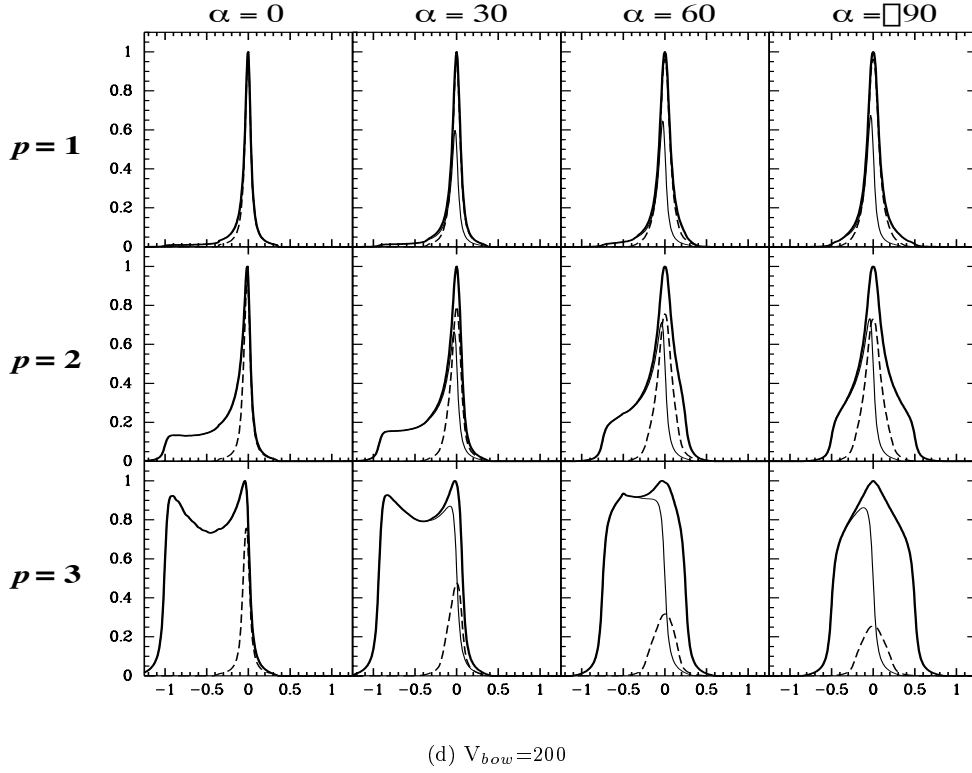
(c) V$_{bow}$=150

(d) V$_{bow}$=200

Figure 8. (continued) As in the previous page, but for bow velocities of 150 and 200 km s^{-1} in panels (c) and (d), respectively. Heavy solid line: no extinction, no dissociation; light solid line: extinction, no dissociation; dashed line: no extinction, dissociation with V$_{lim}$=50.
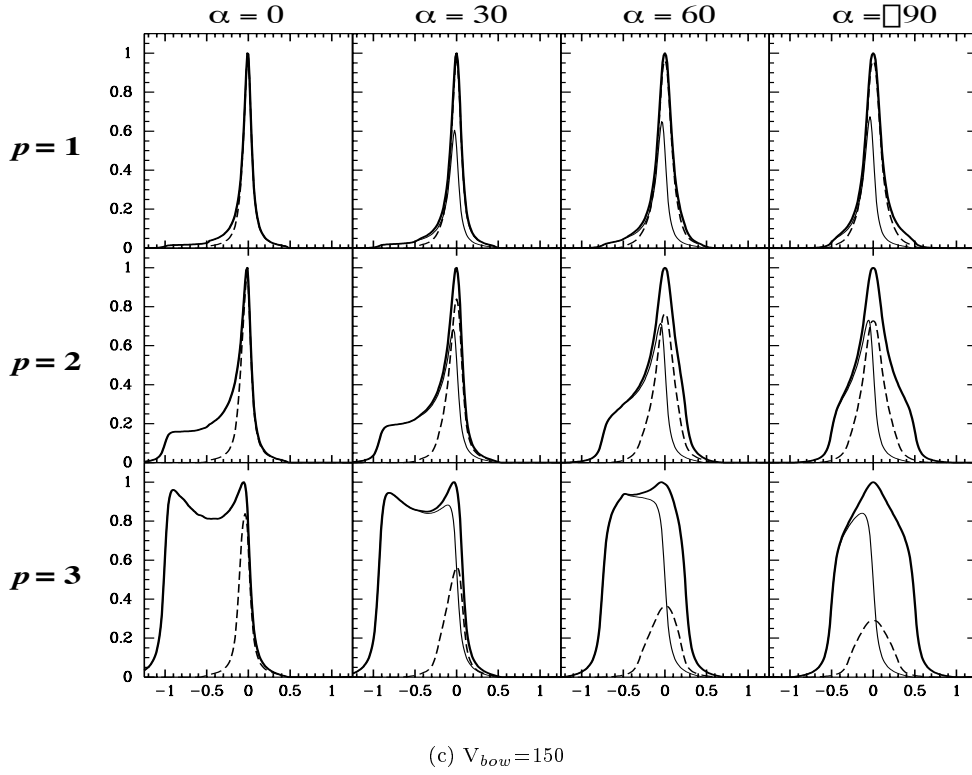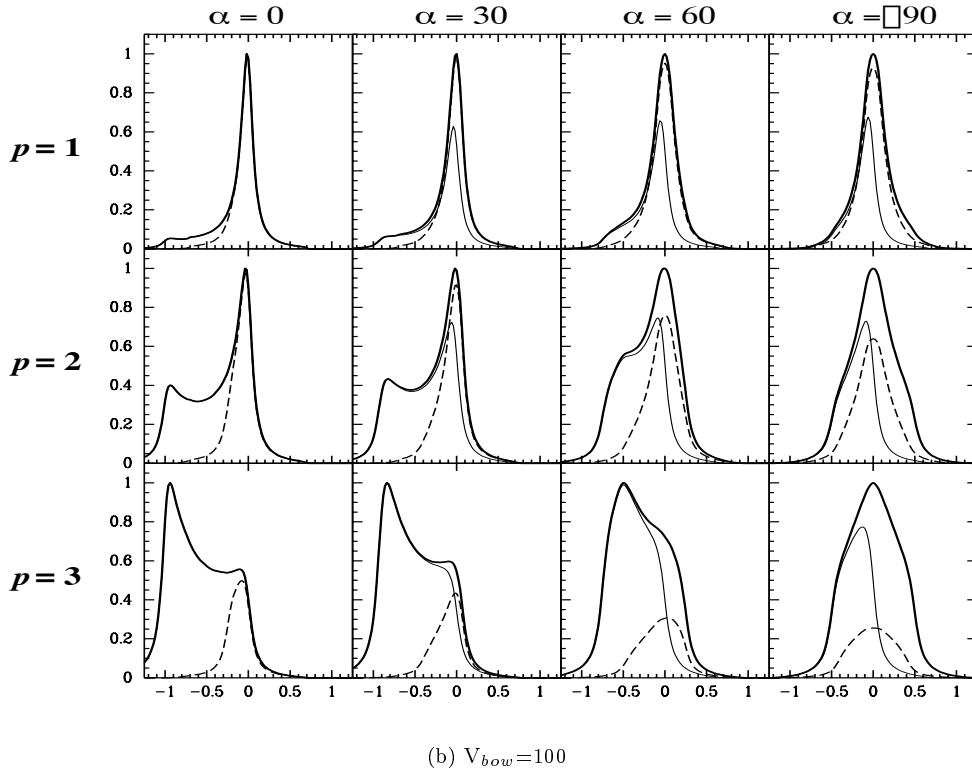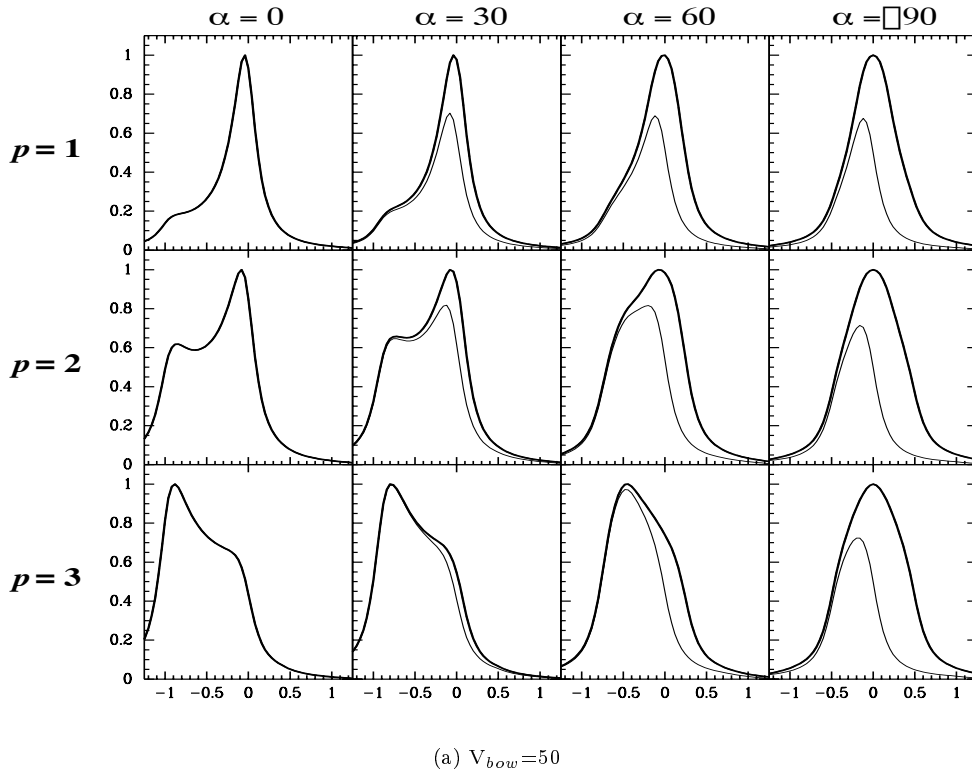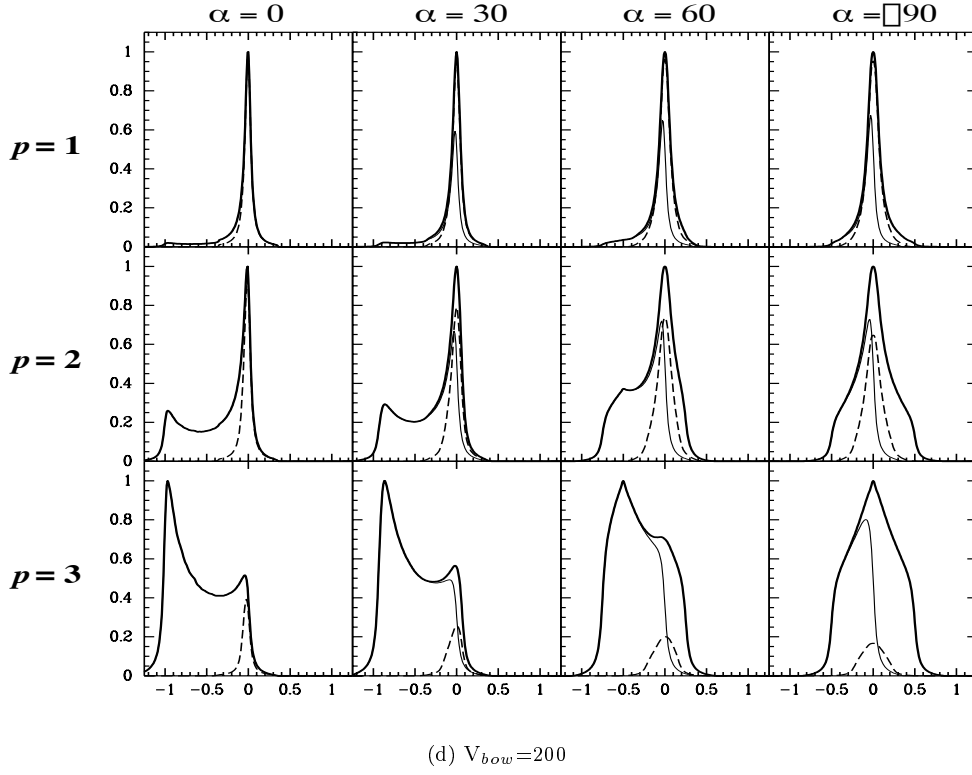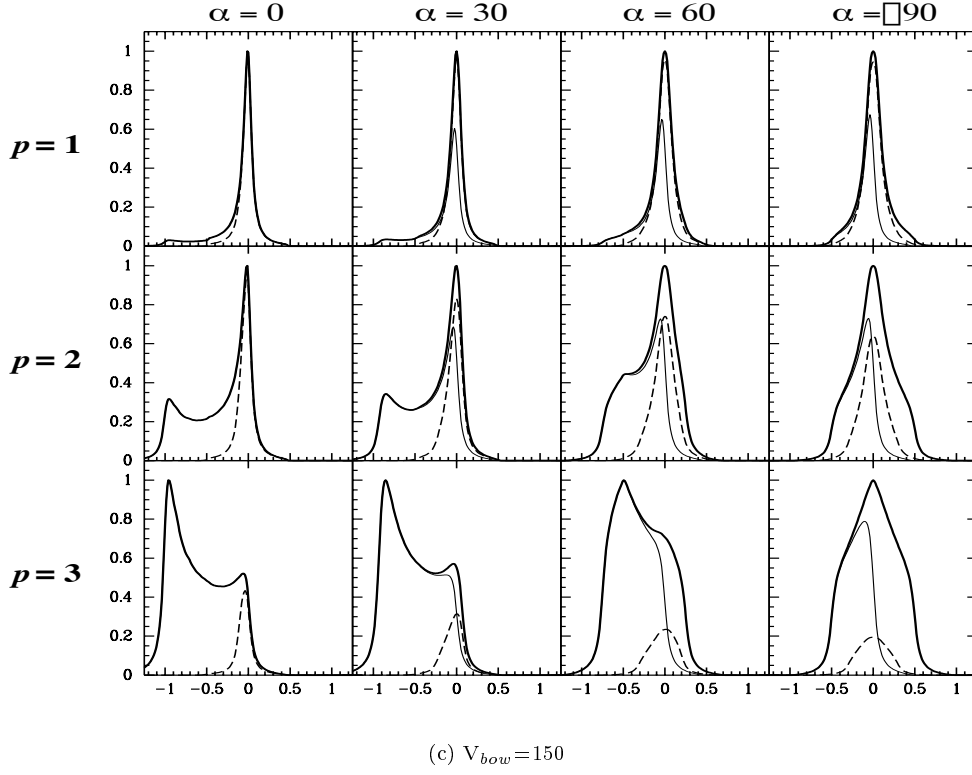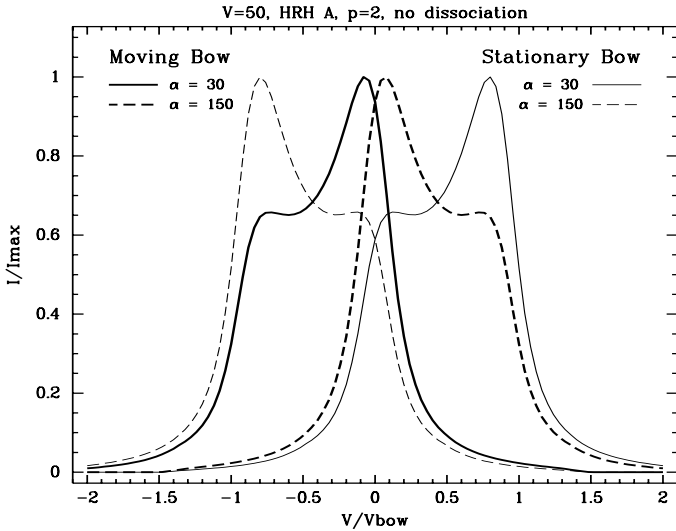
V=50, HRH A, p=2, no dissociation

Figure 9. A comparison of profiles of moving and stationary bows at $\alpha = 30$ degrees (solid lines) and $180 - \alpha = 150$ degrees (dashed lines). The profiles are for an HRH A bow with $V_{bow} = 50$ km s^{-1} and $p = 2$. Moving bow profiles are shown in heavy lines (both solid and dashed); stationary bow profiles in light lines.

line signifies that $V_{lim} = 50$ km s^{-1}, with no extinction; and a light solid line represents a model with extinction, but with no dissociation. The x-axes of the profiles have been normalised to the bow speed to facilitate comparison between models.

We have chosen to omit the case of $V_{lim} = 50$ km s^{-1} with extinction from these plots, for the sake of clarity. The effects can easily be extrapolated from the other three profiles (an example is shown in Fig. 17).

Figures 10, 11, 13, 15 and 16 illustrate the effects of changing a single parameter while holding the others constant. These will be discussed further in their respective sections, below.

The profiles presented here are for a bow moving in a stationary medium, at viewing angles $0 \leqslant \alpha \leqslant 90$ degrees (that is, toward the observer). Bow shocks retreating from us can be modelled by setting $90 < \alpha \leqslant 180$ degrees. The model will also accommodate the case of a stationary bow impacted by a moving medium at a velocity $V_{wind} = -V_{bow}$ (that is, in the positive z-direction).

These cases are illustrated in Fig. 9 for an HRH A bow with $V_{bow} = 50$ km s^{-1} and $p = 2$. The solid lines represent bows with orientation angles of $\alpha = 30$ degrees, the dashed lines bows with $\alpha = 150$ degrees. Heavy lines (both dashed and solid) represent moving bows in a stationary medium, while the light lines represent stationary bows in a moving medium.

The profiles produced by a retreating bow with an orientation angle α are those of an advancing bow at $180 - \alpha$, reflected about $v_r = 0$. This can be seen from Eqn. A9 when $\cos \alpha$ is substituted by $\cos(180 - \alpha) = -\cos \alpha$.

Profiles produced by a stationary bow are the profiles of a moving bow at the same orientation, shifted redward by $V_{wind} \cos \alpha$, as is obvious from Eqns. A7 and A9.

3.1 Effects of the Bow Velocity V_{bow}

The effects of increasing velocity on the profiles are complex, and vary considerably with bow shape (see Fig. 10). An increase in bow speed broadens the profile (this is not readily apparent in Fig. 10, because each profile has its velocity axis normalised to its own bow speed). Increasing velocity also tends to lower the strength of the blue wing relative to the central peak, because at low velocities a greater proportion of the bow surface has $v_\perp < 5$ km s^{-1}, below which molecular hydrogen emission is not excited. As the bow speed increases, emission from the high-velocity gas at the apex also increases, but the bow surface area over which low-velocity gas emits increases faster, thereby strengthening the core of the profile over the wing.

The effects of bow velocity are dependent upon the value of p; at $p = 3$ the flux at the apex often dominates over the effects of the increased emitting area. See §3.3 for more details.

3.2 Effects of Bow Shape

Our model compares four different bow shapes, which are shown in Figure 4. The bluntness at the apex and radius at the "tail" are the primary factors controlling the shape of the line profile. The greater the apex bluntness, the higher the shock velocity ($v_\perp = \sin \psi$) there. A larger radius at the tail means a larger contribution from weakly-shocked gas.

The Raga shape was found by Raga & Böhm (1985), who examined possible bow shapes formed around spherical, rigid bodies moving supersonically through a homogeneous medium. The formulation we use was developed by HRH. Their expression assumes a specific size for the spherical body of 8.4×10^{15} cm (560 AU), which is not unreasonable for a Herbig–Haro object.

HRH Shape A is used in many of the shock models of HRH, who found that it reproduced their observed line profiles (which were from atomic species, rather than H_2).

The effect of shape change, keeping all other variables equal, is to increase the strength of the blue wing relative to the core in the following sequence: parabolic, Raga, cubic, HRH A (see Fig. 11). The reason for this can be seen in Figure 4. Except for the case of $\alpha \approx 90$ (when the bow is seen from the side), the bluest emission will come from the region of the strongest shocks, that is, the apex of the bow. Therefore, the relative strength of the blue wing is controlled by how rapidly the angle ψ – the angle between V_{bow} and the tangent to the bow surface, which approaches 90 degrees near the apex (see Fig. 2) – decreases with increasing z. When ψ is small, the shock is weak and the emission is low, since $v_{shock} = v_\perp = V_{bow} \sin \psi$. For the case of HRH A, ψ decreases more rapidly than in the other bow shapes; hence a larger portion of the HRH A bow contributes relatively little to the resulting profile.

We see from Fig. 4 that ψ decreases less rapidly as one moves from cubic to Raga to parabolic bows. The profiles of the parabolic bow are significantly different from those of the other bow shapes studied, because of that shape's much more gradual curvature. In this case, ψ remains non-negligible at large z, which means that gas far behind the apex will still be weakly shocked and there will be a large

Figure 10. Variation in line profiles as the bow speed varies (V_{bow}=50, 100, 150 and 200 km s⁻¹). All profiles within a single plot are normalised to a common peak intensity, and the velocity axes are normalised to the bow speed in each case. The models display a range of illustrative parameter sets, and the particular bow shapes and values for cooling indices, viewing angles and dissociation limits are indicated in each plot.

area contributing appreciably to the profile at low radial velocities.

While the blue wing is not as prominent in the Raga bows as in the cubic or Shape A bows, it is broader. Fig. 4 shows that the Raga bow has a greater surface area at the apex, where the radial velocities are high. For this reason, it exhibits a broader blue wing which merges with the line core. This is seen in Figs. 11(b) and 11(d).

Parabolic bows are dominated by the emission toward the tail of the bow, which results in simple, single-peaked profiles. In Paper II we will show that such profiles do not fit the observed Orion BN-KL data well.

Fig 12 shows the four bow shapes colour-coded for radial velocity; the shadings represent bows with $V_{bow} = 200$ km s^{-1} at viewing angles $\alpha = 0$, 30, 60, and 90 degrees. The colour scale at the bottom indicates the relation of colour to v_r/V_{bow}. The bows are all drawn on the same scale, and have all been truncated to a length of $z = 3$ to highlight the "interesting" emission near the apex (see §A4 for the significance of truncation of the bows). Note that most of bow surface emits at low radial velocity; the relative contribution of this low-velocity gas to the final profile will depend upon the cooling function index, p (see §A1).

The figure shows that the area of highest radial velocity (represented by dark blue) in the parabolic bow is localised to a region very near the apex, and falls more gradually with z than it does in the other bow shapes. This is consistent with the more gradual slope of the parabolic bow's surface. The other bow shapes have a much more extended region of high-velocity gas, especially the Raga shape. As can be seen in Fig. 4, the Raga bow has a larger apex area than the other shapes. This causes the radial velocity to remain high for a relatively large distance behind the apex, and accounts for the "bridge" betweeen the blue wing and zero-velocity peak in Raga bow profiles (see, e.g. the low-alpha, $p = 3$ profiles in Figs. 7(c) and (d), and compare them to cubic bow profiles with the same parameters in Figs. 6(c) and (d)).

3.3   Effects of the Cooling Function Index p

The effect of increasing the cooling function index, p, is to increase the relative contribution from the regions near the apex of the bow (see Fig. 13). This is because the intensity increases as $v_\perp{}^p$, where $v_\perp = V_{bow}\sin\psi$. Again, ψ is the angle the velocity vector makes with the tangent to the bow surface, which approaches 90 degrees at the apex.

The effect on the line profiles can be dramatic. As p increases, there is a sharp increase in the strength of the the blue wing relative to the core, since a comparatively large amount of emission comes from the apex of the jet – the region with the highest shock velocity. This is true for all profiles where $\alpha \leqslant 90$ deg.

These effects are most easily observed at high velocity, e.g. in Fig. 13(a) or 13(d). As p increases (while keeping α constant), the blue wing becomes more pronounced, finally becoming (in the case of 13(a)) stronger than the core at $p = 3$. Compare Fig. 13(a), with $V_{bow} = 200$ km s^{-1} to Fig. 13(c), which shows the same model except that V_{bow} has been set to 50 km s^{-1}. The increase in blue wing with p is less dramatic in the lower-velocity case.

Figure 14 illustrates the dependence of flux on p for the four bowshapes. The top plot in each subfigure shows the flux per unit area ($V_{wind}^p\sin^p\psi$, where in this case $V_{bow} = 50$ km s^{-1}) – normalised to the flux at the apex of the bow – vs z for the three values of p. The lower plot shows the variation of the area element dA with z (the total flux in an element is $I = f\,dA$; see §A1). Note that for three of the shapes, dA actually *decreases* with z in a region at the head of the bow; this is an indication of the rapid decrease in ψ. As can be seen from Figs. A1 and A2, a steep decrease in ψ (and therefore ds) can offset the increase in R, causing dA to decrease with z. Each of the plots is carried out to $z = z_{term}$, the length a bow attains before the V_{term} of 5 km s^{-1} is reached (see §A4).

The three bows at the side of each plot also display the variation of flux with z. Each bow element is coloured with its unit flux, normalised to the unit flux at the apex; the colour scale indicates the correspondence between colour and normalised flux. The lengths of the bows (distorted somewhat by the viewing angle) reflects z_{term} (the cubic, Raga, and HRH A bows are reproduced on a common scale; the parabolic bows are roughly 2.5 times larger than depicted here, on that scale).

The bow shapes supplement Figs. 11 and 13 by presenting the same information in a more visual form. For example, as p increases, the increasing contribution by the emission at the apex is demonstrated by the increasingly sharp transition between the blue/green areas (representing high intensity emission) and the red areas (representing low intensity emission). The relatively small apex and large tail of the parabolic bow accounts for its simple, wingless profiles. The shallower slope of the Raga bow apex (relative to, e.g., the cubic bow) is responsible for its higher flux levels between the blue wing and the zero-velocity peak.

In Paper II we will show that profiles with dominant blue wings are not observed in BN-KL.

3.4   Effects of the Viewing Angle α

The line profile is also sensitive to changes in α (see Fig. 15). The blue wings of profiles which exhibit them lie at $-V_{bow}\cos\alpha$. When $\alpha = 0$ (i.e. the bow is viewed head on) the peak of the wing will fall at a velocity $-V_{bow}$; the velocity of the peak will move toward zero velocity with increasing α, up to $\alpha = 90$ (i.e., the bow is viewed from the side; see e.g. Fig. 15(d)). At that point the profile is symmetrical about $v = 0$ as long as there is no extinction (see §3.6).

The height and shape of the blue wing will vary with V_{bow}, p and the bow shape (compare Fig. 15(c) to 15(d), which have the same parameters except for the shape). The effects of the change in α on a profile can be substantial when the profile is dominated by high-velocity emission from the apex of the bow. See, e.g., Fig. 8, and note that the change in profile with α is much more pronounced for higher values of p. Compare this with Fig. 5, where the changes due to α are more modest. The profiles of parabolic bows are dominated by low-velocity gas from the rear of the bow, while those of the HRH A bows are dominated by high-velocity gas from the apex of the bow. Fig. 15(a) shows that even in the parabolic case the line peak shifts slightly, from negative velocity to zero as α changes from 0 to 90 degrees.

When $90 \leqslant \alpha < 180$ (i.e. when the bow is pointed *away* from the observer), the results are the same except that the
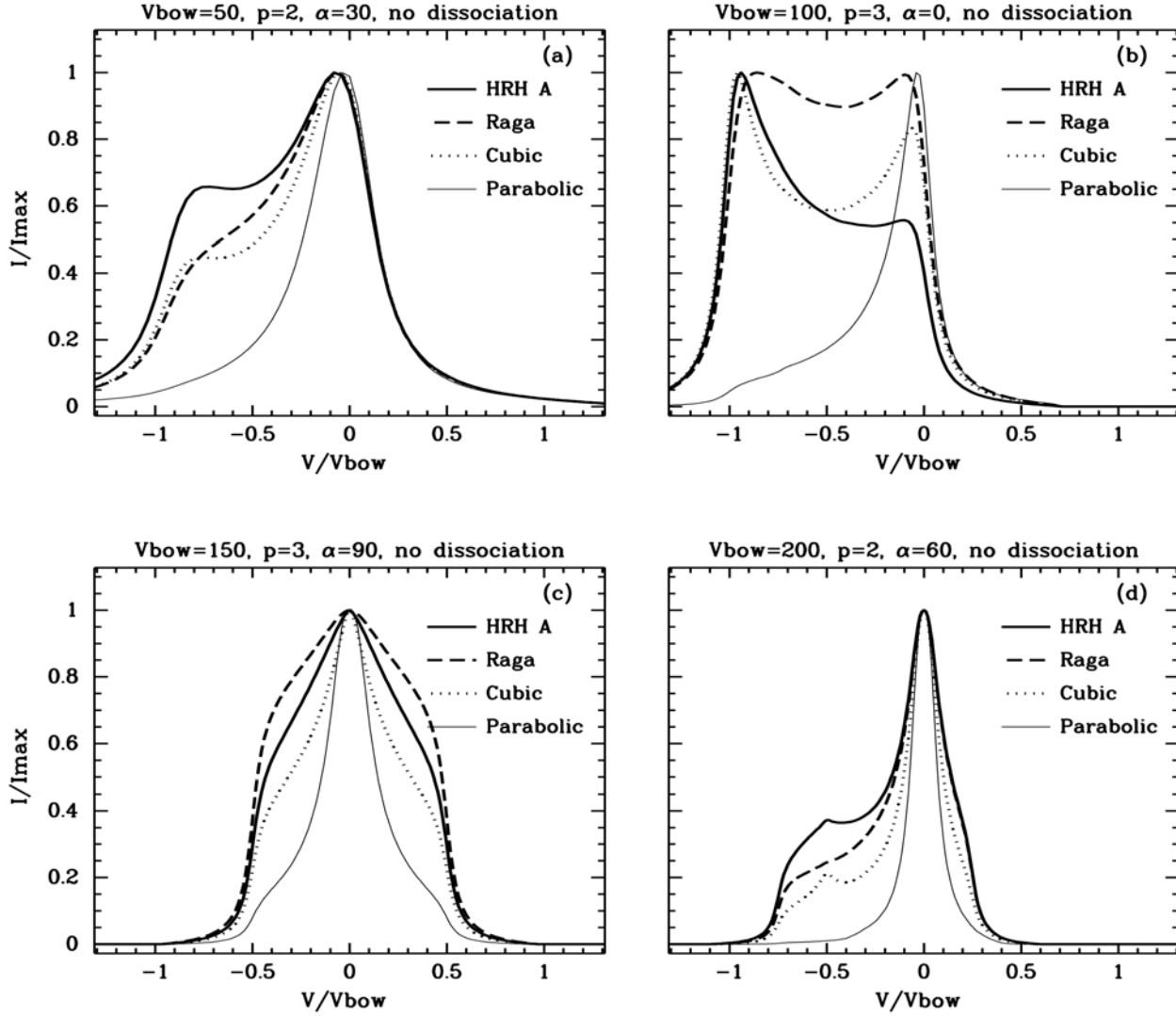
Figure 11. Variation in line profiles as the bow shape varies (parabolic, cubic, Raga and HRH A). All profiles within a single plot are normalised to a common peak intensity, and the velocity axes are normalised to the bow speed in each case. The models display a range of illustrative parameter sets, and the particular values for bow speed, cooling indices, viewing angles and dissociation limits are indicated in each plot.

profiles are reflected symmetrically about zero velocity (i.e. the wings are red rather than blue; see Fig. 9).

3.5 Effects of the Dissociation Limit V_{lim}

We have examined two dissociation cases: no dissociation, and dissociation at a limiting velocity of 50 km s^{-1}. In Figs. 5 through 8 the dissociation case is shown as a dashed line. In plots where there is no dashed line (e.g. for cases with $\alpha = 0$, $p = 1$), dissociation has little effect on the profile. Figure 16 shows the effect of increasing V_{lim}. The $V_{lim} = 200$ km s^{-1} case is equivalent to no dissociation.

The effect of dissociation is to eliminate emission from the part of the bow where $v_{\perp}$ is greatest, i.e. the region around the apex. For $\alpha < 90$, the most obvious result is the suppression of blue wings; when $\alpha = 90$, both red and blue wings are suppressed. The main effect of dissociation,

therefore, is to simplify the profile; the lower the dissociation velocity, the more simple and symmetrical the profile. We see very few such simple profiles in our observations of the bow shocks in Orion BN-KL. This will be discussed in Paper II.

Figure 16(b) clearly shows the suppression of the blue wing, and when compared to the no-dissociation case (the solid line), illustrates the fraction of emission coming from the head of the bow. As may be expected, this fraction is large for larger values of p, since the intensity is proportional to $v_{\perp}^{p}$. Figure 16(c) illustrates the suppression of both wings when $\alpha = 90$. Dissociation is more readily apparent in the profiles for bows which are viewed face-on than for those viewed from the side.
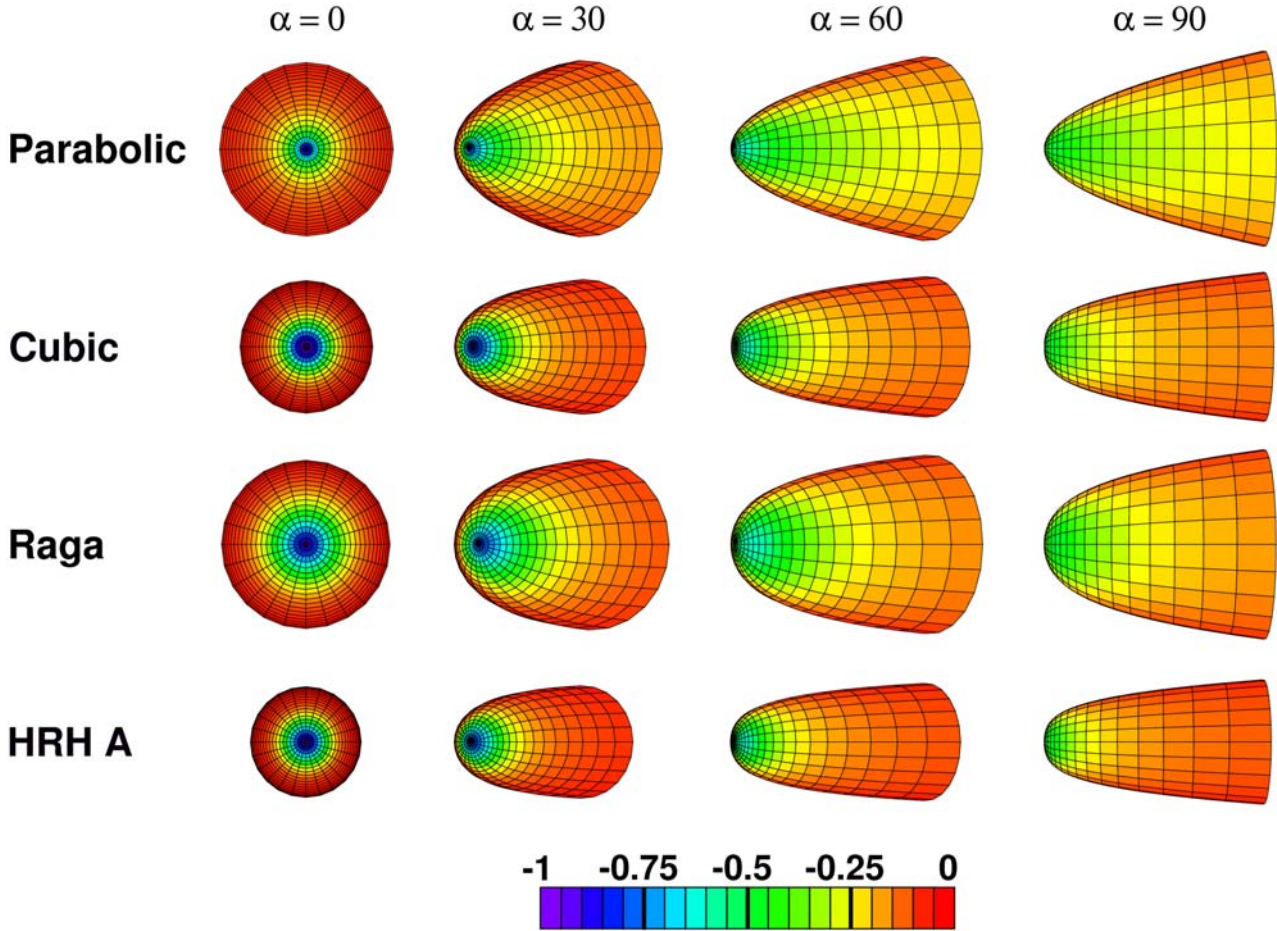
Figure 12. A colour-coded representation of the radial velocity of the emission for the four bow shapes, with $V_{bow} = 200$ km s^{-1} and viewing angle $\alpha = 0$, 30, 60, and 90 degrees. The bows are all drawn on the same scale, but truncated to a length of $z = 3$. The colour scale at the bottom shows the relationship of colour to v_r/V_{bow}.

3.6   Effects of Extinction

Finally, we have studied two extreme cases of extinction: no extinction, and total extinction within the bow. This assumes dust within the hollow bow completely blocks emission from gas not directly visible to the observer. For example, at $\alpha = 30$, some small part of the "far" side of the bow, near the apex, is directly visible, and only emission from this portion is not blocked. Extinction cannot be properly treated without adopting specific physical bow parameters, such as size, but examining the two extreme cases gives an indication of how partial extinction will affect observed line profiles.

Figures 5 through 8 show the effects of extinction as profiles drawn in a light solid line. These effects can be most easily seen in high-velocity cases at $p = 3$, such as 6(d) or 7(d), simply because the shape of the profiles allows the extinction curve to be seen easily. The extinction effect varies, of course, with α. Extinction has no effect at $\alpha = 0$, when the bow is head on, because all the bow surface is directly observed. At low viewing angles (e.g., $\alpha = 30$) the effect begins to be noticeable as a slight decrease in intensity at the reddest velocities. At these small angles, the blocked emission from the back side of the bow is at low (positive) velocities,

and low intensities, so its absence does not change the profile very much. The suppression of the positive-velocity emission increases with increasing α; at $\alpha = 90$, the entire red wing of the profile is eliminated. (Our curves show a small amount of emission at positive velocities because of the smoothing that has been applied.)

While the case of extinction with dissociation has been omitted from Figs. 5 through 8, an example of its effects is presented in Fig. 17. The effect of extinction alone for this model is a reduction in the zero-velocity gas while the blue wing remains prominent; the effect of dissociation alone is a drastic suppression of the blue wing, leaving a simple, single-peaked profile. The results of adding extinction to the dissociation model is therefore a simple profile centred at low negative velocities, in which the emission from the zero velocity gas has been suppressed.

4   CONCLUSIONS

We have presented a simple model for H$_2$ line profiles in bow shocks moving through a stationary medium at a velocity V_{bow}. The model takes into account the effects of bow speed, bow shape and viewing angle. We also examine changes in
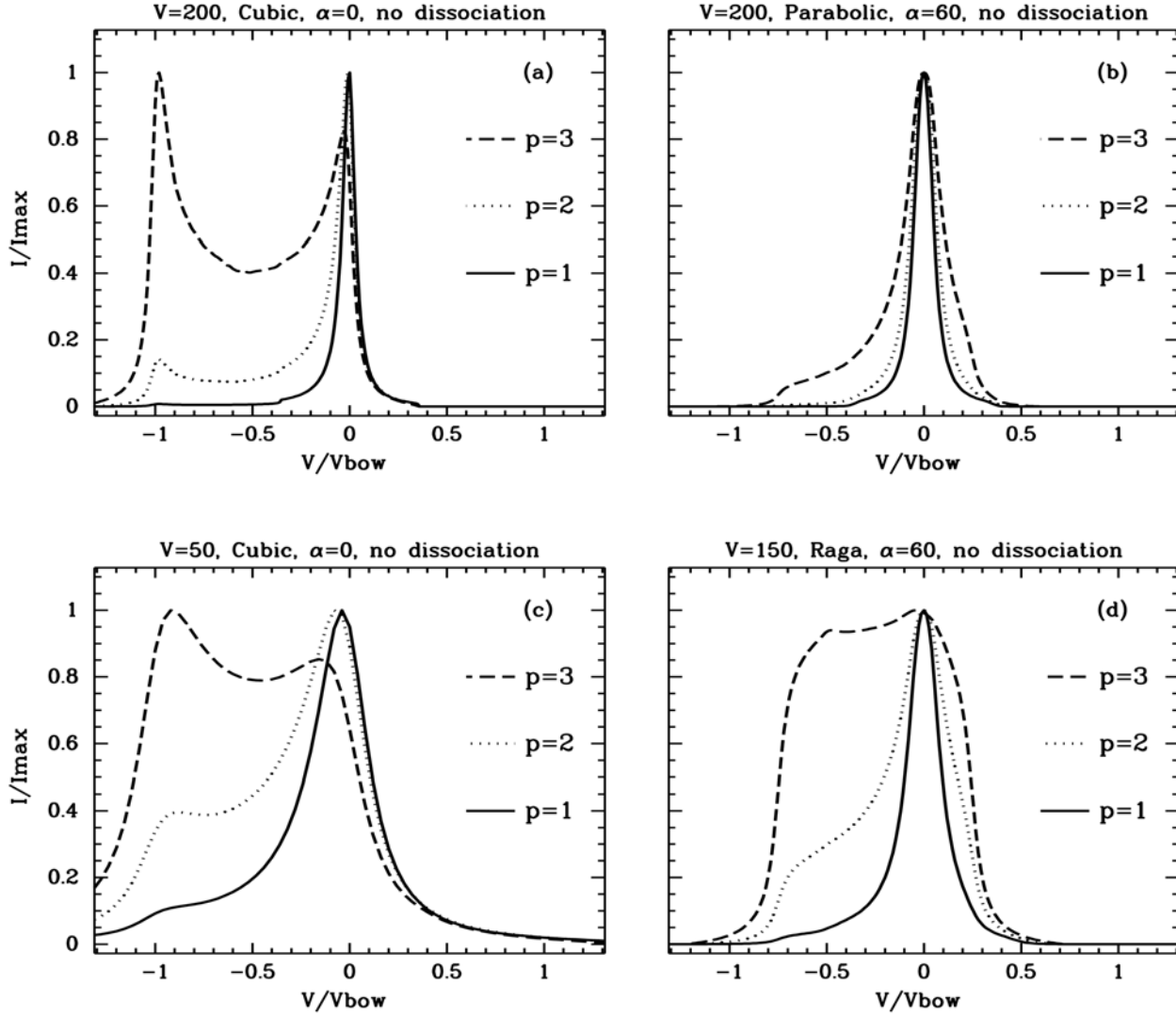
Figure 13. Variation in line profiles as the cooling function index varies ($p = 1$, 2 and 3). All profiles within a single plot are normalised to a common peak intensity, and the velocity axes are normalised to the bow speed in each case. The models display a range of illustrative parameter sets, and the particular bow shapes and values for bow speed, viewing angles and dissociation limits are indicated in each plot.

the cooling function index, p, which accounts for the amount of energy released into the emission line. In addition, we investigate the effects of dissociation, and of extinction within the bow.

More specifically we find that:

• An increase in bow velocity broadens the line profile by moving the blue wing further from the core.

• The cubic, Raga and HRH A bow shapes give generally similar line profiles. The Raga bow profiles tend to exhibit a "bridge" of emission between the blue wing and line core, because of its larger apex area and more gradual curvature there. Profiles of parabolic bows are markedly different, due to the contribution from a large area of weakly-shocked gas at the rear of parabolic bows.

• An increase in the cooling function index, p, increases

the strength of the blue wing relative to the core and can lead to dramatic changes in line profiles.

• Generally, the profile narrows with increasing α as the blue wing moves closer to the core. At $\alpha = 90$ degrees (i.e., the bow is seen side-on), the line profile becomes symmetrical about zero velocity. The peak of the blue wing, which is produced by shocked gas at the bow apex, will lie at $-V_{bow} \cos \alpha$.

• Dissociation suppresses the emission from gas with the highest shock velocity (i.e., near the apex of the bow), thus weakening the blue wing of the profile for bows with low values of α. When the bow speed is much larger than V_{lim}, the effect of dissociation is to eliminate the blue wing altogether, thus producing a very simple profile. This effect is particularly pronounced when the cooling function index is high.

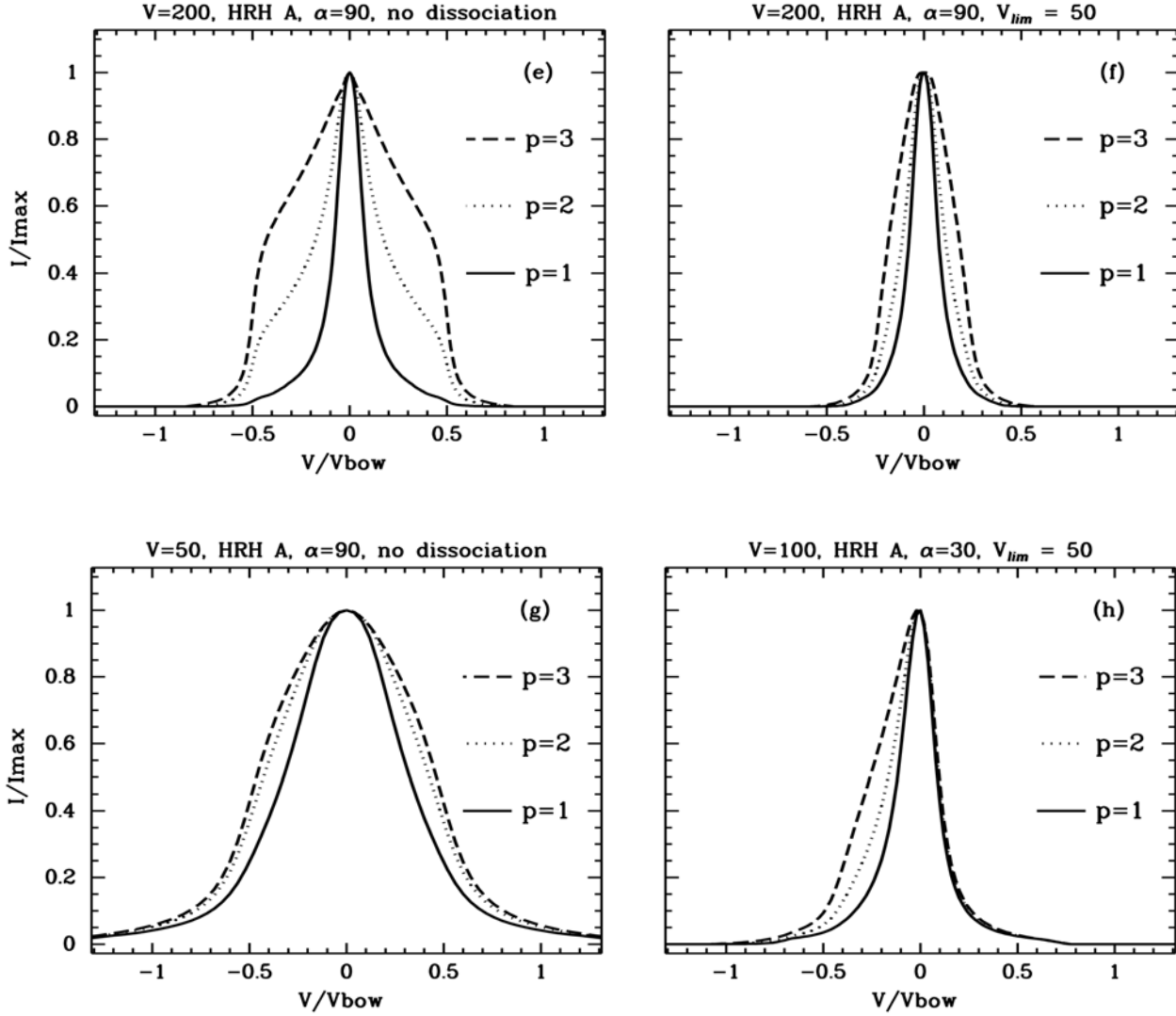• Total extinction within the hollow bow will tend to sup-

Figure 13. (continued) Variation in line profiles with cooling function index, p.

press the red portions of the profile, leaving (in many cases) an asymmetric profile shifted toward the blue.

The model has a number of limitations. We are not constraining the bow to a specific physical size, and therefore do not include the gas density in our models. This means that we cannot directly compare flux measurements between different parameter sets, or to observations.

Presently, most of the chemistry of the model is bound up in the cooling function index, p, a crude indicator of the amount of kinetic energy which is translated into line emission. In reality, p would vary over the shock front as a function of temperature and density, as well as the composition of the medium. Likewise, the dissociation velocity will not be uniform throughout the shock, but will vary with density and magnetic field.

The present method of modelling extinction demands that the material within the bow be thick enough to completely obscure emission from the far side of the bow. In order to correctly model the extinction, we would have to adopt a specific size and density distribution for the bow.

The model may readily be extended to examine bow shocks which are spatially resolved, in order to compare the relative emission from different parts of the same bow shock. Current observational data are not sufficient to examine this, but as integral field units are developed to study emission lines at high spatial and spectral resolution, and proper motion measurements constrain the 3D motions, such a comparison may be warranted in the future. A special case – truncation of the length of the bows – is discussed in §A4.

In Paper II we will compare our models to data obtained from Fabry-Perot observations of the bow shocks in the Orion BN-KL outflow. We will find that most of the observed bows are fit best by models with higher V_{bow} with no dissociation, and lower values of p.

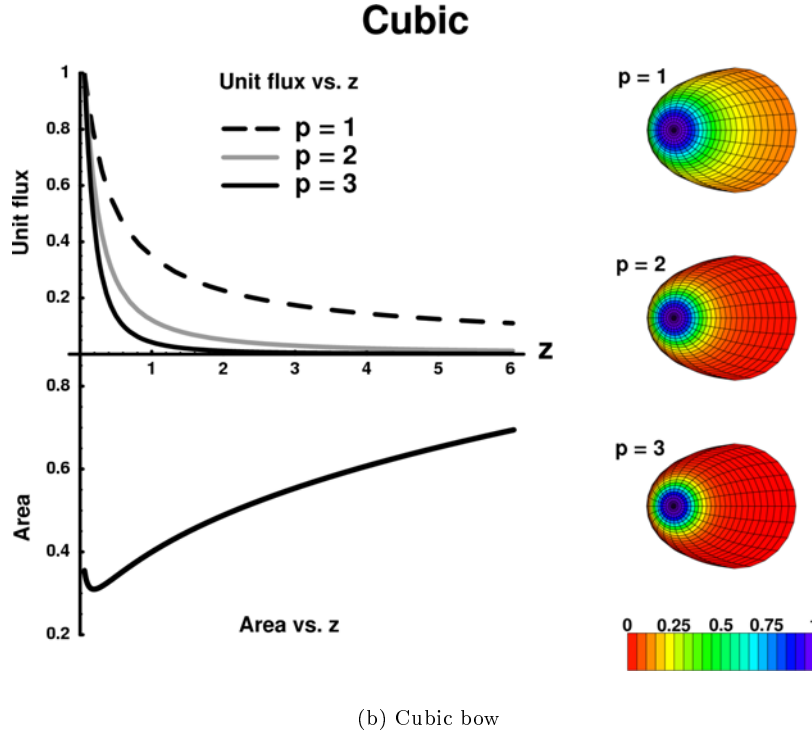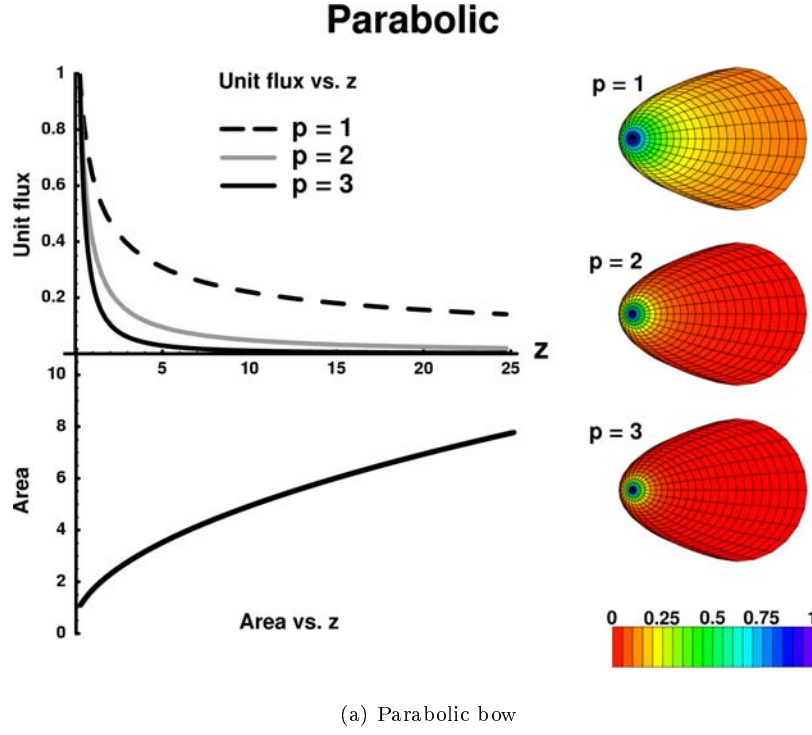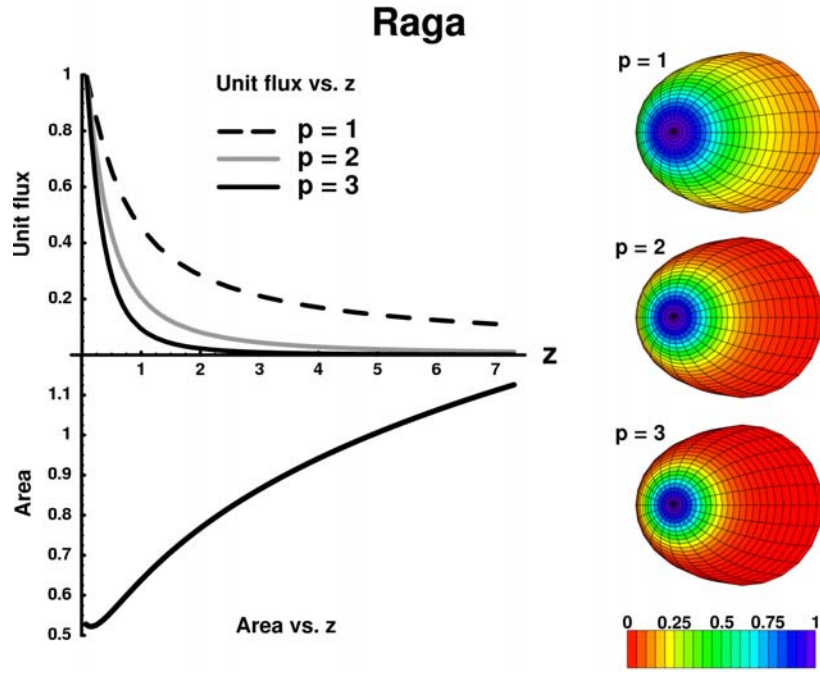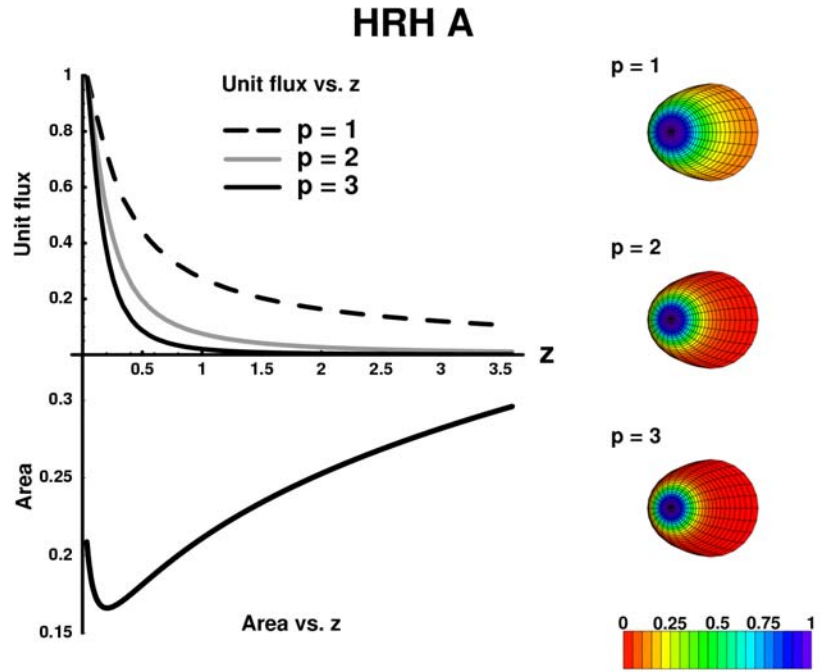(a) Parabolic bow

(b) Cubic bow

Figure 14. An illustration of the variability of flux and element area with distance along the bow, z, for a parabolic bow (a) and a cubic bow (b), both with $V_{bow} = 50$ km s^{-1}. The upper plot shows the variation with z of the flux per unit area, normalised to the flux per unit area at the apex. The three curves represent the three values of the cooling index, p. The lower curve plots the variation in bow element area dA with z. The three coloured bows illustrate the bow shape, with colour indicating the level of the normalised flux per unit area. The scale at the bottom shows the relation of colour to unit flux. See text for further details.

(c) Raga bow

(d) HRH A bow

Figure 14. (continued) As in the previous page, except for Raga (c) and HRH A (d) bow shapes.
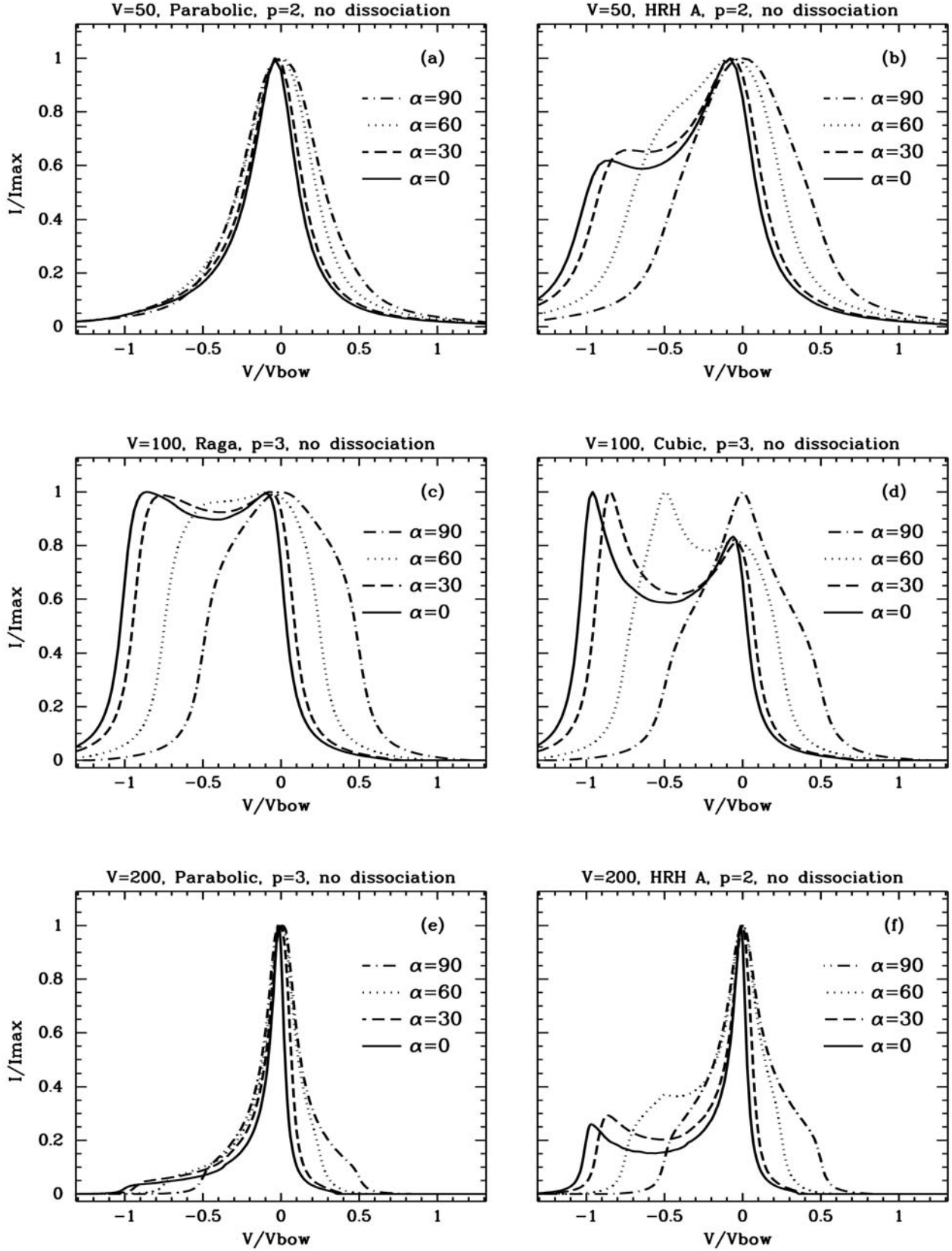
Figure 15. Variation in line profiles as the viewing angle, α, varies ($\alpha = 0$ (face-on), 30, and 60, and 90 degrees (side-on)). All profiles within a single plot are normalised to a common peak intensity, and the velocity axes are normalised to the bow speed in each case. The models display a range of illustrative parameter sets, and the particular bow shapes and values for bow speed and cooling index are indicated in each plot.
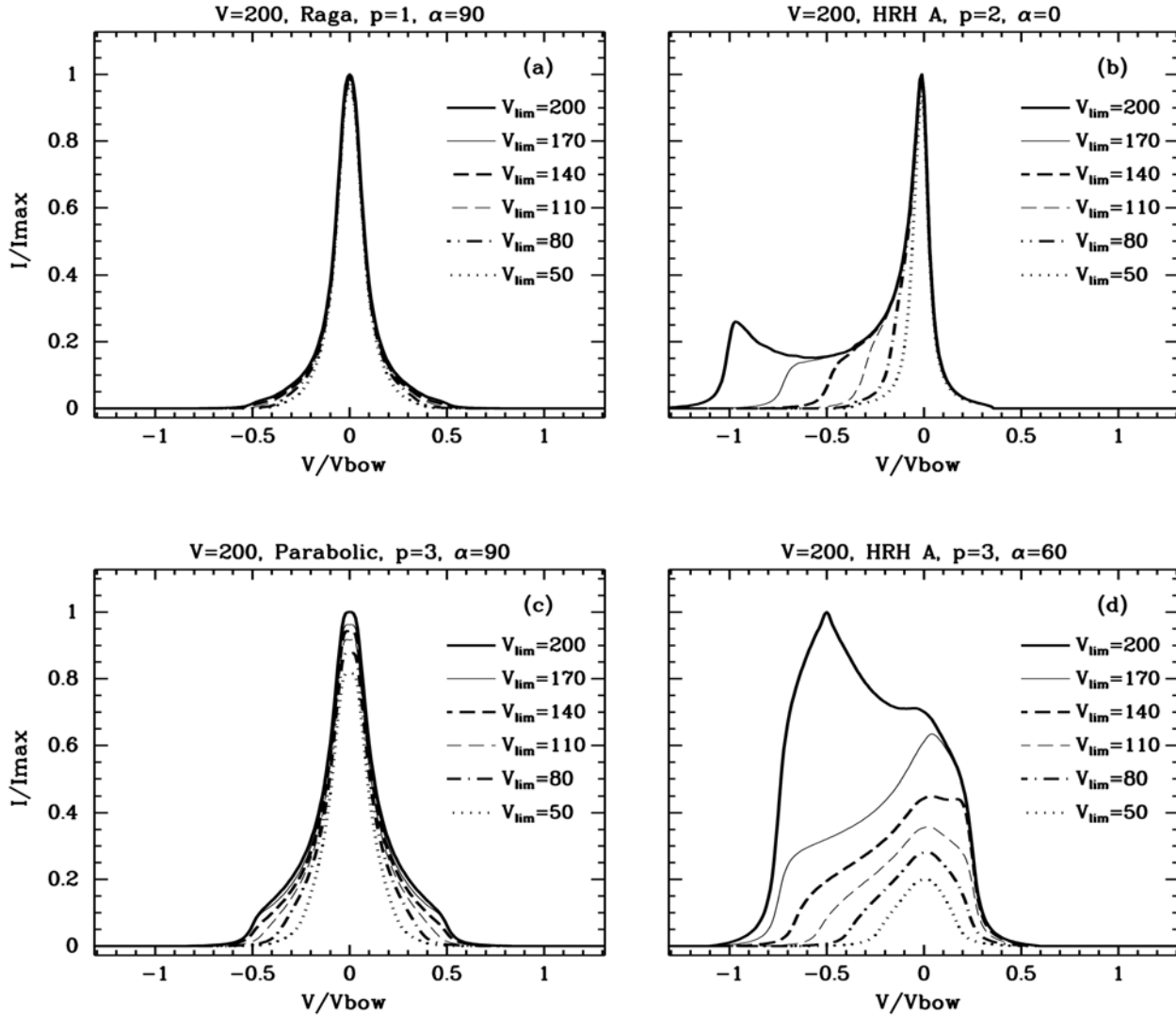
Figure 16. Variation in line profiles as the dissociation speed varies (V_{lim}=50, 80, 110, 140, 170 and 200 km s^{-1}). All profiles within a single plot are normalised to the peak intensity of the $V_{lim} = 200$ (no dissociation) curve, and the velocity axes are normalised to the bow speed in each case. The bow speed for all bows is 200 km s^{-1}. The models display a range of illustrative parameter sets, and the particular bow shapes and values for cooling index and viewing angle are indicated in each plot.

REFERENCES

Allen D.A, Burton M.G. 1993, Nature, 363, 54

Bally J., Heathcote S., Reipurth B., Morse J., Hartigan P., Schwartz R. 2002, AJ, 123, 2627

Bucciantini N., Bandiera R. 2001, A&A, 375, 1032

Burton M.G., Hollenbach D.J., Tielens A.G.G. 1992, ApJ, 399, 563

Draine B.T, Roberge W.G., Dalgarno A. 1983, ApJ, 264, 485

Hartigan P., Raymond J., Hartmann L. 1987, ApJ, 316, 323 (HRH)

Heathcote S., Morse J.A., Hartigan P., Reipurth B., Schwartz R.D., Bally J., Stone J.M. 1996, AJ, 112, 1141

Noriega-Crespo A., van Buren D., Dgani R., 1997, AJ, 113, 780

Markevitch M., Gonzalez A.H., David L., Vikhlinin A.,

Murray S., Forman W., Jones C., Tucker W. 2002, ApJ, 567, 27

Mundt R., 1985, in Black D.C., Matthews M.S., eds, Protostars and Planets II. Univ. Arizona Press, Tucson, p. 414

Norman C., Silk J. 1979, ApJ, 228, 197

Raga A.C., Böhm K.-H., 1985, ApJS, 58, 201

Raga A.C., Böhm K.-H., 1986, AJ, 92, 119

Reipurth B., Heathcote S., Morse J., Hartigan P., Bally J. 2002, AJ, 123, 362

Schultz A.S.B., Colgan S.W.J., Erickson E.F., Kaufman M.J., Hollenbach D.J., O'Dell C.R., Young E.T., Chen H. 1999, ApJ, 511, 282

Schwartz R.D. 1978, ApJ, 223, 884

Smith M.D., Brand P.W.J.L., Moorhouse A. 1991, MNRAS, 248, 730
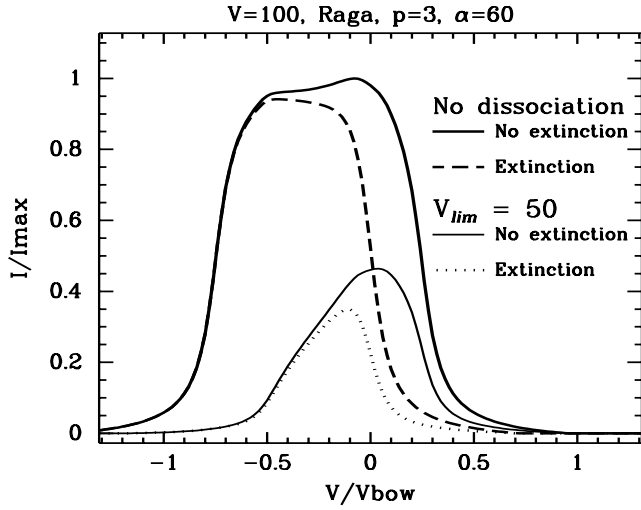
Smith M.D., Khanzadyan T., Davis C.J., 2003, MNRAS,

Figure 17. The effects of extinction and dissociation are illustrated using a Raga shape with $V_{bow} = 100$ km s^{-1}, cooling index $p = 3$, and viewing angle $\alpha = 60$ degrees. No extinction or dissociation, heavy solid line; extinction with no dissociation, dashed line; no extinction with dissociation at $V_{lim} = 50$ km s^{-1}, light solid line; extinction with dissociation at $V_{lim} = 50$ km s^{-1}, dotted line. Other model parameters are as indicated. All curves are normalised to the peak of the no extinction, no dissociation curve, and the velocity axis has been normalised to the bow speed.

339, 524

Spreiter J. R., Stahara S. S. 1995, AdSpR, 15, 433

Stolovy S.R. et al. 1998, ApJ, 492, 151

Stone J.M., Xu J., Mundy L.G. 1995, Nature, 377, 315

Taylor K.N.R., Storey J.W.V, Sandell G., Williams P.M., Zealey W.J. 1984, Nature, 311, 236

Vázquez, R., López-Martín L., Miranda L.F., Esteban C., Torrelles J.M., Arias L., Raga A.C. 2000, A&A, 357, 1031

APPENDIX A: MATHEMATICAL APPENDIX

In our model the bow shape is divided into a number of elements in z, the longitudinal axis of the bow, and ϕ, the azimuthal angle about the z-axis. The flux, I, and radial velocity v_r of each element are calculated by the methods given below in §A1 and §A2, respectively.

Because the mathematics are more easily visualised for a stationary bow in a moving medium, Figs. A3 and A4 illustrate this case. The results in the main body of the paper are for a moving bow in a stationary medium.

If the user chooses to include the effects of extinction, some elements on the "far" side of the bow will not be visible to the observer. The extinction routine (§A3) determines which elements are obscured and omits them from the calculations.

The results in the main body of the paper are for bows which have reached a length z_{term}, the point where the shock velocity has become so low that hydrogen molecules are no longer excited. We assume this velocity to be 5 km s^{-1}. In §A4, we discuss the effects on the line profile if the bow is truncated to a length $z < z_{term}$.

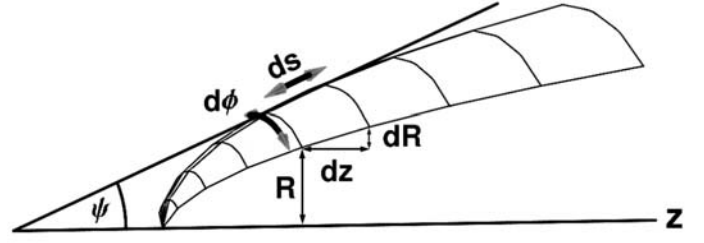In order to facilitate plotting, the radial velocity range

of each bow is divided into a number of bins. This number can have an effect on the final profile, as described in §A5.

A1 Flux

The flux in an element is $I = f \, dA$, where dA is the area of an element, and f is the flux per unit area in that element.

The derivation for the size of the area element is illustrated in Fig. A1. The line element ds, at a radius R above the z-axis, is swept through an angle $d\phi$ to give the area dA:

$$dA = R \, ds \, d\phi \qquad (A1)$$

The length element ds is assumed to be small enough to be approximated by a straight line, as shown in Fig. A2. This line is tangent to the bow surface at the position R, and makes an angle ψ with the z-axis such that $\tan\psi = \frac{dR}{dz}$. The length of ds, then, is just $dz/\cos\psi$, where the value of dz is chosen by the user. The final expression for dA is given by

$$dA = \frac{R \, d\phi \, dz}{\cos\psi} = \frac{R \, dR \, d\phi}{\sin\psi}, \qquad (A2)$$

remembering that R is a function of z which depends on the chosen bow shape.

The flux per unit area, f, is given by $f = n_0 v_\perp{}^p$. As explained in §2, p is the cooling function index, which is a measure of how much of the shock energy goes into producing a single emission line. In the current model, n_0 is set to 1. Therefore, $f = v_\perp^p = V_{wind}^p \sin^p\psi$, which yields

$$I = V_{wind}^p \, R \, d\phi \, dz \frac{\sin^p\psi}{\cos\psi}. \qquad (A3)$$

A2 Radial Velocity

Although the profiles we have presented all involve a bow moving through a stationary medium, the mathematics is more easily understood in terms of a stationary bow in a moving medium. The conversion to a moving bow then involves a simple change of reference frame, as seen below in Eqn A9.

The stationary bow is struck by a wind with velocity $\mathbf{V_{wind}}$, moving in the positive z-direction (see Fig. A3). At the bow surface, $\mathbf{V_{wind}}$ is resolved into components normal to the bow, $\mathbf{v}_\perp = V_{wind} \sin\psi \, \hat{\mathbf{n}}$, and tangential to the bow, $\mathbf{v}_\parallel = V_{wind} \cos\psi \, \hat{\mathbf{t}}$, where $\hat{\mathbf{n}}$ and $\hat{\mathbf{t}}$ are the unit vectors in
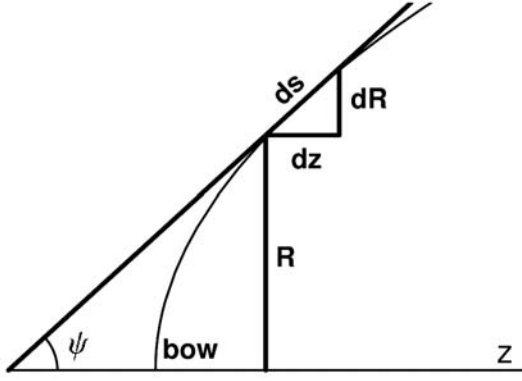

Figure A1. Illustration of area calculations. The length segment ds is swept through an angle $d\phi$ to give the surface area dA of a bow segment.

Figure A2. Calculation of the length of the segment ds.

the directions normal and tangential to the bow surface, respectively:

$$\hat{\mathbf{n}} = -\cos\psi\cos\phi\;\hat{\pmb{\imath}} - \cos\psi\sin\phi\;\hat{\pmb{\jmath}} + \sin\psi\;\hat{\mathbf{k}}, \qquad (A4)$$

and

$$\hat{\mathbf{t}} = \sin\psi\cos\phi\;\hat{\pmb{\imath}} + \sin\psi\sin\phi\;\hat{\pmb{\jmath}} + \cos\psi\;\hat{\mathbf{k}}. \qquad (A5)$$

It is important to remember that ϕ is defined as being measured from the positive x-axis toward the positive y-axis.

We assume that $\mathbf{v}_\perp$ becomes zero in the post-shock gas (see §2), so that the only remaining gas velocity is $\mathbf{v}_\parallel$. The radial velocity, therefore, will be the component of $\mathbf{v}_\parallel$ which lies along the line of sight. The unit vector, $\hat{\mathbf{a}}$, along the line of sight is given by

$$\hat{\mathbf{a}} = \sin\alpha\;\hat{\pmb{\imath}} + \cos\alpha\;\hat{\mathbf{k}}, \qquad (A6)$$

where α is the angle the line of sight makes with the z-axis. The observed radial velocity will then be

$$
\begin{aligned}
v_r &= \hat{\mathbf{a}} \cdot V_{wind}\cos\psi\;\hat{\mathbf{t}} \\
&= V_{wind}\cos\psi(\sin\alpha\sin\psi\cos\phi + \cos\alpha\cos\psi). \qquad (A7)
\end{aligned}
$$

Again, this is for the case of a stationary bow in a moving medium. If instead the medium is at rest and the bow is moving, we must add the speed of the bow along the line of sight

$$v_r = \hat{\mathbf{a}} \cdot V_{wind}\cos\psi\;\hat{\mathbf{t}} + \mathbf{V_{bow}} \cdot \hat{\mathbf{a}}, \qquad (A8)$$

where $\mathbf{V_{bow}} = -V_{wind}\;\hat{\mathbf{k}}$, since the bow is travelling in the $-z$ direction. Therefore the radial velocity for a moving bow in a stationary medium is

$$
\begin{aligned}
v_r = V_{wind}[&\cos\psi(\sin\alpha\sin\psi\cos\phi + \cos\alpha\cos\psi) \\
&- \cos\alpha]. \qquad (A9)
\end{aligned}
$$

A3   Extinction

In the extinction case we assume total extinction within the bow – that is, we discard the emission from all bow elements which are not directly visible to the observer. When $\alpha = 0$, the bow is face on, so all of it is visible and no emission is discarded. When $\alpha = \pi/2$, exactly half the bow is visible, that half for which $\phi = \pi/2$ to $3\pi/2$. For all other values of α, the range of visible ϕ depends on z and α.

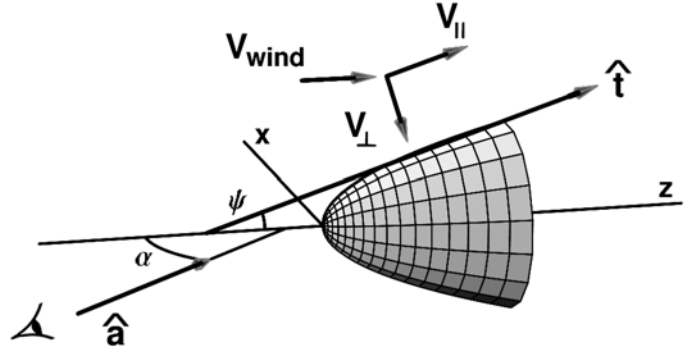Fig. A4 shows the appearance of the bow to an observer

Figure A3. Illustration of vectors for the v_r calculations. The y-axis has been omitted for clarity.

when $\alpha = 30$ degrees. Only those elements which are visible in the figure will be computed when α has this value. The portion of the bow which will be discarded is shown in Fig. A5, in which the bow and observer are viewed from a position on the positive y-axis. The elements to be discarded are shown in black (the view is symmetrical about the x-z plane).

The region of the bow which is hidden begins where the line of sight is tangent to the bow surface, where $\hat{\mathbf{a}} \cdot \hat{\mathbf{n}} = 0$. We must find ϕ_{tan}, the value of ϕ where this occurs.

$$
\begin{aligned}
0 &= \hat{\mathbf{a}} \cdot \hat{\mathbf{n}} \\
&= -\sin\alpha\cos\psi\cos\phi_{tan} + \cos\alpha\sin\psi
\end{aligned}
$$

$$\cos\phi_{tan} = \tan\psi\cot\alpha$$

or

$$\phi_{tan} = \arccos\left(\frac{dR}{dz}\cot\alpha\right) \qquad (A10)$$

There are two solutions to this equation: ϕ_{tan} and $2\pi - \phi_{tan}$. These angles mark the points on the bow where $\hat{\mathbf{a}} = \hat{\mathbf{t}}$. All elements whose ϕ values fall outside this range are discarded.

We see in Eqn. A10 that ϕ_{tan} is a function of z. Therefore, in addition to depending upon ϕ, the location of the discarded elements depends upon z. Bow elements are not discarded unless they fall outside the range $\phi_{tan} \to 2\pi - \phi_{tan}$, *and* their z-coordinate is $z > z_{tan}$.

In order to determine z_{tan}, we return to Eqn. A10. Since the cosine of any angle cannot be outside the range ±1, there are regions on the bow where there is no solution to Eqn. A10; the entire bow is visible in these regions. We must find the point where there first is a solution for Eqn. A10.

This point, z_{tan}, can be found by setting $\cos\phi_{tan} = 1$. For the parabolic bow, for example:

$$\cos\phi_{tan} = 1 = \cot\alpha\left.\frac{dR}{dz}\right|_{z=z_{tan}} \qquad (A11)$$

therefore

$$
\begin{aligned}
\tan\alpha &= \left.\frac{dR}{dz}\right|_{z=z_{tan}} = \left.\frac{1}{2R}\right|_{z=z_{tan}} \qquad (A12) \\
&= \frac{1}{2\sqrt{z_{tan}}}
\end{aligned}
$$

so that finally

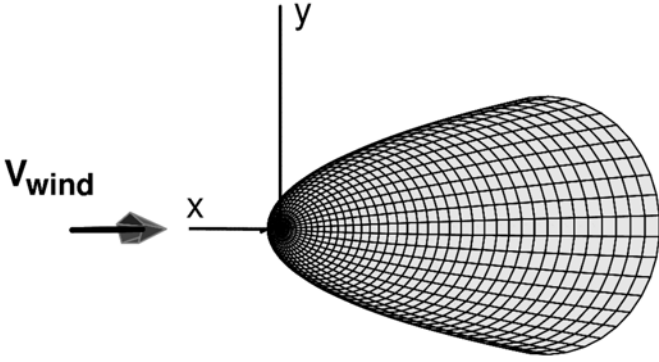$$z_{tan} = \frac{\cot^2\alpha}{4}. \qquad (A13)$$

Figure A4. Bow from the viewpoint of the observer when $\alpha = 30$ degrees.
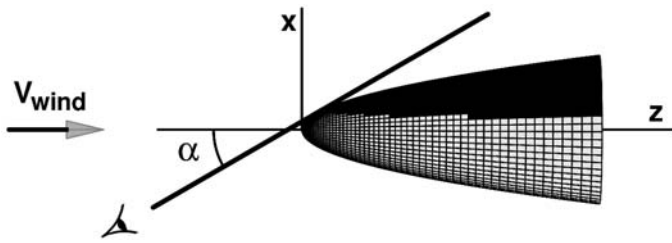

Figure A5. Bow and observer from the positive y-axis, showing blocked region of the bow when $\alpha = 30$ degrees and extinction is used. The thick line at viewing angle α represents the observer's line of sight and is tangential to the bow.

The value of z_{tan} is used to set the range of ϕ values for which intensities will be calculcated. When $z < z_{tan}$, ϕ will step from $0 \rightarrow 2\pi$; otherwise the allowed values of ϕ are $\phi_{tan} \rightarrow 2\pi - \phi_{tan}$. Fig. A6 displays the change in z_{tan} and ϕ_{tan} as α increases.
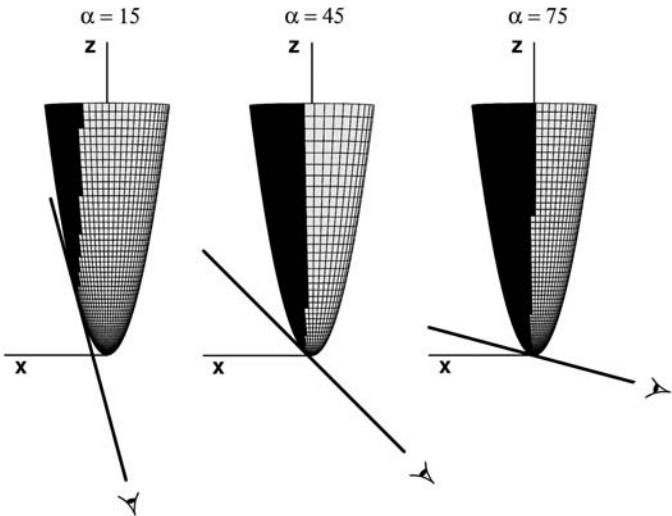

Figure A6. As in Fig. A5, but for $\alpha = 15$, 45 and 75 degrees.

A4 Truncation of the Bow

As explained in §2, we have assumed that the gas will no longer be excited once $v_\perp$ falls below $V_{term} = 5$ km s^{-1}. The distance along the bow axis where this occurs, $z = z_{term}$, depends on V_{bow} and bow shape. It is important to ensure that the chosen bow length is not less than this distance, if we wish to examine the emission from the entire bow. The value of z_{term} can be found by setting $v_\perp = V_{term} = V_{bow} \sin\psi$. Since $\tan\psi = \frac{dR}{dz}$:

$$V_{term} = V_{bow} \sin\left(\arctan\frac{dR}{dz}\right)\Big|_{z=z_{term}}$$

$$= V_{bow} \frac{\frac{dR}{dz}}{\sqrt{1+(\frac{dR}{dz})^2}}\Big|_{z=z_{term}} \tag{A14}$$

where $\frac{dR}{dz}$ is a function of z dependent upon bow shape. Solving Eqn. A14 for z yields z_{term}. For example, for the parabolic bow

$$V_{term} = V_{bow} \frac{\frac{1}{2\sqrt{z}}}{\sqrt{1+(\frac{1}{2\sqrt{z}})^2}}\Big|_{z=z_{term}} \tag{A15}$$

so that

$$z_{term} = \frac{1}{4}[(\frac{V_{bow}}{V_{term}})^2 - 1]. \tag{A16}$$

The effects of bow truncation on the line profile can be seen in Fig. A7. In both plots, the light solid line represent the profile expected from a bow which has been allowed to extend out to z_{term}; the other profiles are for bows which have been truncated before reaching this point. The effect of bow truncation is to reduce the contribution from low shock-velocity gas at the tail of the bow. This is more important at lower values of p, where the contribution from the tail is greatest. Especially in the parabolic case, truncation can change a simple profile into a double-peaked one, as seen in Fig. A7.

Fig. A8 shows the relative sizes of the four bow shapes when the bows have been allowed to extend to z_{term} for $V_{bow} = 100$ km s^{-1}. Because of its comparatively gradual decrease in ψ, z_{term} is much larger for parabolic bows than for the other bow shapes, especially when V_{bow} is large. This means that parabolic bows extending to z_{term} have a large fineness ratio (length/maximum diameter) compared to the other shapes. The large fineness ratio exhibited by the parabolic bow in Fig. A8 is not seen in astronomical bow shocks, and the ratio will increase with increasing V_{bow} (the latter is true for the other shapes as well). Therefore, if the observed bow shocks are found to have bow speeds greater than ≈ 50 km s^{-1}, some process must truncate them to a length less than z_{term}, and this must be taken into consideration when interpreting line profiles. The values of z_{term} and fineness ratios for the four bow shapes and standard values of V_{bow} are shown in Table A1.

A5 Binning

As described above, the bow is divided into a number of elements in both ϕ and z. The velocity range of the resultant profile (which is taken to be $4V_{bow}$) is also divided into bins of width dv, a value chosen by the user. As I_i and v_{r_i} are
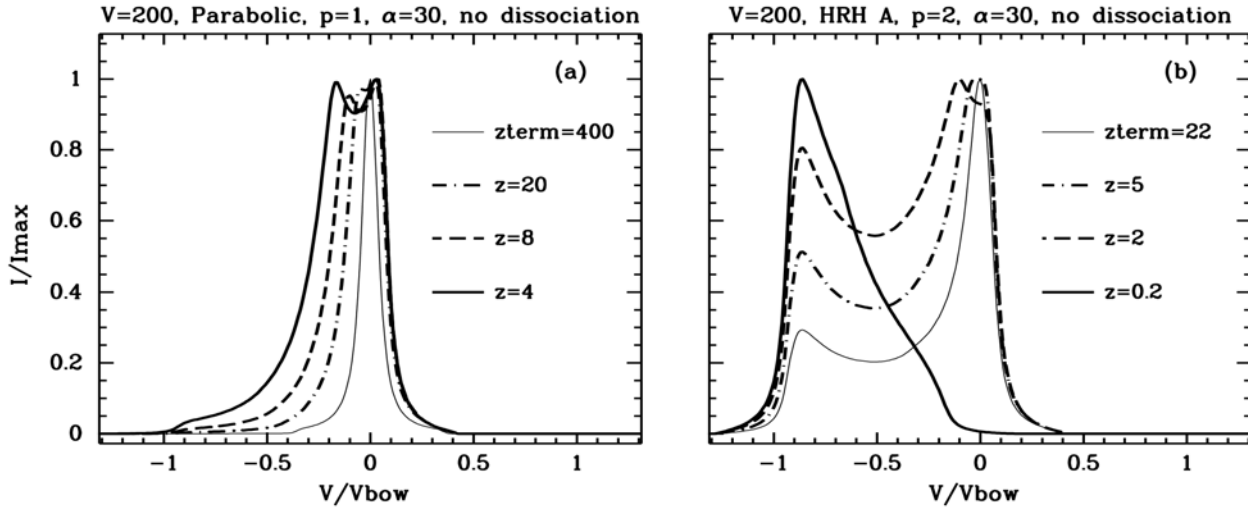
Figure A7. Variation in line profiles with decreasing bow length for parabolic (a) and HRH A (b) bows, with other bow parameters as indicated. In each case the light solid line indicates the profile expected from a bow of length z_{term}, the point at which $v_\perp$ falls to $V_{term} = 5$ km s^{-1}. Each curve is normalised to its own peak intensity, and velocity axis is normalised to V_{bow}.

Table A1. Values of z_{term} and fineness ratio ($f.r. = z_{term}/$maximum diameter) for the four bow shapes and standard values of V_{bow}.

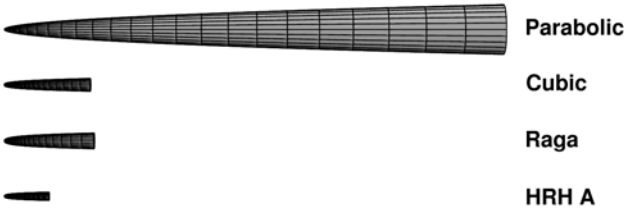| V_{bow} (km s^{-1})	Parabolic		Cubic		Raga		HRH A	
	z_{term}	$f.r.$	z_{term}	$f.r.$	z_{term}	$f.r.$	z_{term}	$f.r.$
50	24.8	2.5	6.0	1.6	7.3	1.5	3.6	1.4
100	99.8	5.0	17.2	3.3	17.9	2.8	8.9	2.7
150	224.8	7.5	31.6	5.0	30.3	4.1	15.2	4.0
200	399.8	10.0	48.7	6.7	44.1	5.4	22.1	5.2

Figure A8. A comparison of the sizes of the four bow shapes when the bows are of length z_{term}, for $V_{bow} = 100$ km s^{-1}.

calculated for each element i, the value of I_i is added to the velocity bin which contains v_{r_i}. This is done to limit the size of the output, and to facilitate plotting. As we will see, the number of elements calculated can run into the tens of thousands, at minimum.

The choice of the number of ϕ elements ($nphimax$), the size of the z elements (dz), and the width of the velocity bins (dv) can have a significant effect on the line profile. The effect of quantisation in the algorithm employed may result in numerical errors if these quantities are poorly chosen. Fig. A9 shows the effect of increasing the size of dv, keeping the size of the ϕ and z elements constant. The profile is (relatively) smooth at $dv = 4.0$, but becomes coarser as dv increases, although the general morphology of the profile remains unchanged. We have chosen $dv = 2.0$ for our models

(to which a 14 km s^{-1} smoothing has been applied), and do not find that the profile changes for smaller values.

It is a different matter for the case of dz. Fig. A10 shows the effect of increasing dz from 0.1 to 0.002, while $nphimax$ is held constant at 1000 and dv is held constant at 2.0 km s^{-1}. The profile is again relatively smooth for $dz = 0.005$, but exhibits structure for $dz = 0.02$, and has divided into a series of peaks for $dz = 0.05$.

The profile is much less sensitive to changes in $nphimax$. Fig. A11 shows that the profile remains largely unchanged when $nphimax$ is decreased from 100 to 30. It is only when $nphimax$ is further decreased to 10 that the profile is materially altered.

The reason for these effects is the relation between dv and dz or $d\phi$. When the size of the element is large, emission from areas of the bow with a relatively large range of v_r will be placed in a single velocity bin, v_i. The emission from the next z-element will then be placed in a second bin, v_j, whose velocity is much greater than v_i. All the bins between v_i and v_j will be empty. This produces the "quantised" effect seen in Fig. A10.

The effect is more pronounced for z than for ϕ because v_r depends more strongly upon ψ (which is to say, ultimately on z) than upon ϕ (see Eqn. A9). The effect of the choice of dz is seen most strongly at low values of α, when the profile is dominated by emission from the apex of the bow. This is also where the value of ψ changes rapidly.

On the other hand, the results of the choice of $nphimax$

are most pronounced as α approaches 90 degrees, as can be seen from Eqn. A9:

$$
\begin{aligned}
v_r = & \quad -V_{wind} \sin^2 \psi & \text{for } \alpha = 0 \\
= & \quad V_{wind} \cos \psi \sin \psi \cos \phi & \text{for } \alpha = 90
\end{aligned}
\tag{A17}
$$

The dependence of v_r on ϕ is greatest when α is large, note that Fig. A11 is for a bow with $\alpha = 90$ degrees, rather than $\alpha = 0$ degrees as in Fig. A10.

Both variables have their greatest effect for $p = 3$, when the intensity depends on $\sin^3 \psi$. The models presented in this paper use $dz = 0.002$ and $nphimax = 1000$. We did not find that increasing the number of elements materially changed the appearance of the profiles.
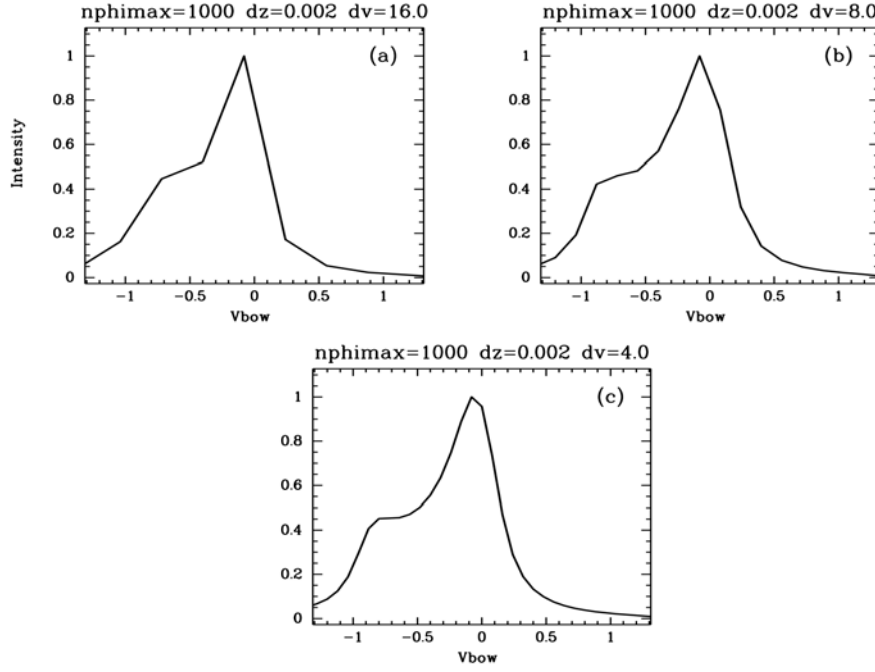
Figure A9. Effect of the change in dv from 16.0 to 4.0 for an HRH A bow with $V_{bow} = 200$ km s^{-1}, $p = 3$, $\alpha = 0$ and with no dissociation or extinction.
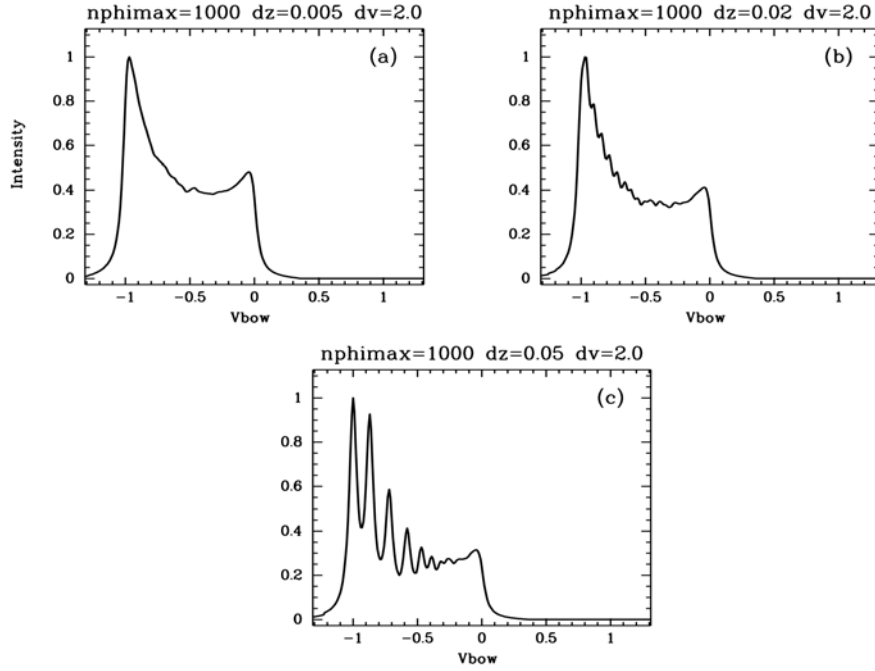

Figure A10. Effect of the change in dz from 0.005 to 0.05 for an HRH A bow with $V_{bow} = 200$ km s^{-1}, $p = 3$, $\alpha = 0$ and with no dissociation or extinction.
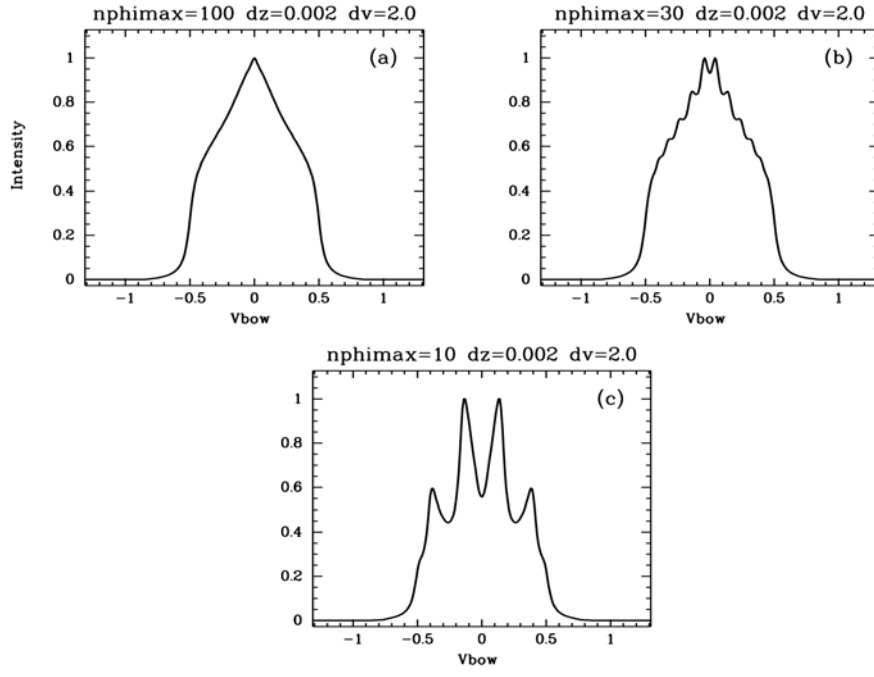
Figure A11. Effect of the change in *nphimax* from 100 to 10 for an HRH A bow with $V_{bow} = 200$ km s^{-1}, $p = 3$, $\alpha = 90$ and with no dissociation or extinction.